9-19-2013

Investigation of Subsonic and Supersonic Flow Characteristics of an Inductively Coupled Plasma Facility

Silas Smith
University of Vermont

INVESTIGATION OF SUBSONIC AND SUPERSONIC FLOW CHARACTERISTICS OF AN INDUCTIVELY COUPLED PLASMA TORCH

A Thesis Presented

by

Silas F. Smith

to

The Faculty of the Graduate College

of

The University of Vermont

In Partial Fullfillment of the Requirements
for the Degree of Master of Science
Specializing in Mechanical Engineering

May, 2013

Accepted by the Faculty of the Graduate College, The University of Vermont, in partial fulfillment of the requirements for the degree of Master of Science, specializing in Mechanical Engineering.

Thesis Examination Committee:

Douglas G. Fletcher, Ph.D. — Advisor

Darren L. Hitt, Ph.D.

Walter J. Varhue, Ph.D. — Chairperson

Domenico Grasso, Ph.D. — Dean, Graduate College

Date: March 22, 2013

Abstract

Inductively Coupled Plasma (ICP) facilities create high enthalpy flows to recreate atmospheric entry conditions. Although no condition has been duplicated exactly in a ground test facility, it is important to characterize the condition to understand how close a facility can come to doing so. An ICP facility was constructed at the University of Vermont for aerospace material testing in 2010. The current setup can operate using air, carbon dioxide, nitrogen, and argon to test samples in a chamber. In this work we investigate different ways to increase measured heat flux and expand our facility to operate supersonically. To do so, a water cooled injection system was designed to overcome failure points of the prior system. An investigation of heat flux methods that provide a baseline for the facility were also examined and tested. A nozzle configuration was also developed with an overall goal of increasing the plasma flow to reach sonic and supersonic velocities, allowing it to be compared with the existing subsonic system. An iterative approach was taken to develop a nozzle design that is robust enough to handle the harsh environment, yet adaptable to the pre-existing facility components. The current design uses interchangeable sonic and supersonic nozzles which also allow for appropriate plasma gas expansion. Data are taken through retractable and goose-neck probe sample holders during testing. Heat flux can be determined by use of a Gardon gage, slug calorimeter, and water cooled calorimeter. Total and static pressure are determined from a pitot tube and pressure tap, which are then manipulated into a velocity measurement. A comparison between subsonic and supersonic operation is then made with these data. Existing literature uses correlations between jet diameter and velocity gradients to determine the effective heat flux. This investigation found that the experimental and theoretical heat flux results scale correctly according to the correlations.

Acknowledgements

I would like to thank my advisor, Dr. Douglas Fletcher for his willingness to support my work throughout my graduate studies at UVM. Special thanks to Walt Owens for giving a hand whenever I needed to carry out an experiment. To everyone in the ICP lab - Dr. Fletcher, Walt Owens, Max Dougherty, Andrew Lutz, Juergen Uhl, and Jason Meyers, thank you for your help and guidance. I would also like thank the Perkins office for providing laughs and always something new throughout the workday.

Thanks to the grant funding that made my research possible,

NASA-NNX11AR69G

NASA-NNX12AL63G

AFOSR-FA9550-11-1-0201

Table of Contents

List of Tables

List of Figures

Chapter 1

Introduction

1.1 Background

Any object moving faster than the local speed of sound will have a shock wave either attached as an oblique shock, or detached as a bow shock in front. Compression behind the shock wave raises the gas temperature, which leads to dissociation and ionization of the gas at high speeds. These hot gases generate large heat fluxes as they flow over the vehicle surface. During an atmospheric reentry, velocities ranging from 6km/s to 15km/s are common depending on trajectory. The corresponding Mach number's are typically much greater than 5; this condition is said to be in the hypersonic regime. Higher flight Mach number's correspond to a stronger shock wave. A Mach number of 25 being typical for an Earth entry, behind the shock wave, the kinetic energy of the vehicle is recovered in the form of temperature and pressure. A massive pressure increase also makes the temperature spike giving the air molecules energy. If this jump in molecular energy is too high then the molecules can dissociate. Dissociation requires energy, but the energy absorbed can be regained at the surface through recombination of the dissociated

molecules. This action releases heat to the surface beyond that of normal convective heating. Therefore, efforts are made to design *non-catalytic* surfaces that do not promote surface recombination.

In the early years of studying hypersonic flight, a sharp nose geometry was the initial design based on missile nose cone aerodynamics. A hypersonic vehicle with a sharp nose would have an attached shock wave, subjecting it to a massive amount of heat focused on the nose tip. Efforts were focused on spreading the heating out over a larger area to minimize local heating rates. As reentry vehicle design evolved, the research converged to blunt nose geometries that promote a detached bow shock.

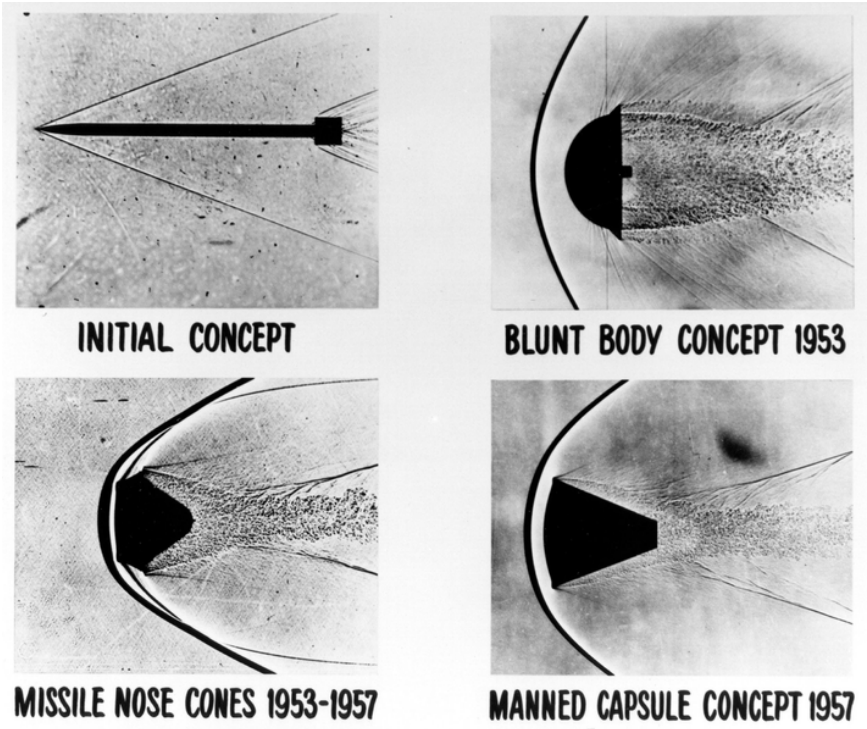

Figure 1.1: The progression of reentry geometry design beginning with missile nose cones to blunt nose objects. [32]

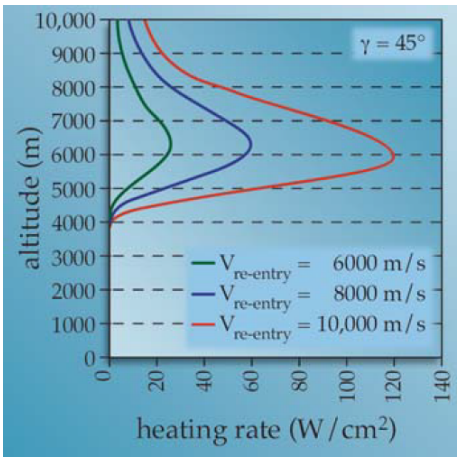

Figure 1.2: Typical heating rate profiles vs. altitude for a few entry velocities. [19]

The velocity V, nose radius, r_{nose}, and density ρ, of the atmosphere dictate the heat flux $\ddot{q}$ on the surface of a reentry vehicle. Figure 1.2 shows three different entry velocities and their corresponding heating rate profiles. Note that in the equation shown below that describes figure 1.2, velocity is to the third power, making it the dominating component, whereas increasing the radius of the vehicle's nose will help reduce velocity as well as spreading the heat over a larger area. The equation below is derived from Allen and Eggers, showing a large velocity dependence.

$$\ddot{q} \cong 1.83 \times 10^{-4} V^3 \sqrt{\frac{\rho}{r_{nose}}}$$

[19],[2]

Figure 1.3 shows different components of heat arriving and leaving the surface for an abating material. The first two are aerodynamic convection and radiation, which have a strong dependence on the body geometry and the angle of reentry. Temperature will rise behind a shock wave promoting radiation that can reach the surface of the vehicle. Locally hot gases will transport dissociated gas particles to the surface through convection. Some literature argues that it is difficult to make the distinction between conduction and convection just above the body's surface.

Most agree that conduction can be considered at the stagnation point, but convection dominates for off-stagnation flows. Energy is required to dissociate gas behind a shock wave, but surface catalyzed recombination of these gases will release heat to the surface if promoted by falling velocity gradients. This can also occur in the material itself if it is porous. Recombination in the gas phase and solid phase are a function of material properties and the atmospheric makeup. The next four components actually remove heat from the ablating surface, obviously at a slower rate, but they are still notable. When the body's surface becomes very hot, a significant amount of energy can be radiated away from any type of surface, and because the nose of the body is pushing the oncoming gases, some of the opposing velocity is used as a blocking mechanism. While for a porous ablator, pyrolyzed gases flow out of the body and block some of the convection. The material vaporization and sublimation both require energy, thus effectively cooling the body.

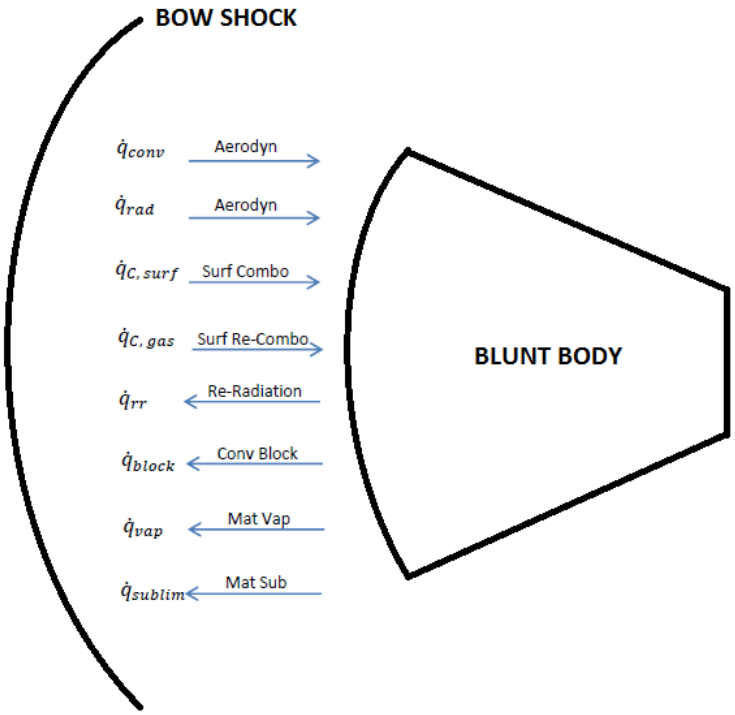

Figure 1.3: Surface heating component breakdown of a blunt nose body for an ablating material.

A well designed thermal protection system (TPS) is needed to protect the vehicle from overheating. Unfortunately, few materials are capable of this challenge, and before they are considered, they are vigorously tested in ground based facilities. Due to the complexity and cost of these facilities, relatively few are deemed "fully" functional.

To perform a good simulation of a reentry, many aspects need to be addressed. Today's state of the art facilities still cannot replicate all of the flight environment characteristics needed to be examined during a simulation in one facility. There are a few different types of reentry ground test facilities capable of partially simulating flight conditions. Arc-jets use a series of stacked copper disks to support a long direct arc that heats the gas. They typically run through a converging diverging

nozzle creating supersonic flow. The benefits being that they produce very high heat fluxes, and they can operate for a long duration. The downside is that the electrodes are placed in the flow and electrode material is boiled off at the attachment points. This material contaminates the plasma stream with material not in the flight environment. Shock tubes, shock tunnels, and ballistic ranges can simulate aerodynamics of reentry, but they do not operate long enough to reproduce the thermal loads. Inductively Coupled Plasma facilities provide electrodless means for heating and dissociating a gas to near flight conditions. ICP's are typically run subsonically, although they can be modified with a nozzle to run supersonically, but at a relatively low Mach number. Today there isn't a single technique or facility that can encompass all components of a reentry, but for a small scale facility, ICP testing is a electrodless way to produce a relatively high heat flux with a small power consumption.

1.2 Exisiting ICP Facilities

The VKI Plasmatron in Belgium is the largest ICP facility in the world. The facility has an installed power of 1.2 MW with an operating frequency of 400 kHz. Operating pressures can fall anywhere from 2 to 13 kPa. The torch uses a 160 mm outlet flow diameter, and there are multiple optical view ports and test probes available. The maximum flow rate is 3000 m^3/h and test duration is 20 minutes or longer. Stagnation point heat flux levels range from 40 to 300 W/cm^2. The Plasmatron is also capable of producing supersonic conditions with a M = 2.3. VKI also uses a 15 kW ICP torch as a pilot for the Plasmatron. The "mini torch" has similar characteristics as the Plasmatron, but on a smaller scale [11].

The Institute of Space Technology and Aeronautics in Japan uses a 110 kW ICP torch in parallel studies with their 750 kW arc-jet. The ICP facility presently has an enthalpy of 20 MJ/kg and a corresponding heat flux of 100 W/cm^2. Operation frequency can range between 1.5 and 3.0 MHz. The plasma torch has an outlet diameter of 80 mm and a mass flow rate of 1.5 to 6 g/s [40]. The University of Stuttgart in Germany also has a strong ICP testing program based on the PWK1 to PWK5 high enthalpy wind tunnels. All five units have different characteristics, but similar when scaled to those previously mentioned.

It should be mentioned that plasma facilities are not all used for thermal protection systems. Tekna Plasma is a company that produces different ICP torch units for fine particle coating application. One of the main differences is that their units operate at atmospheric pressure and some are capable of supersonic plasma operation. A study at the Plasma Technology Research Centre, University of Sherbrooke was made using the a 20 kW ICP torch developed by Tekna plasma to test temperature profiles in a plasma. The setup involved 3 nozzles, the first designed for Mach 3, the second for Mach 1.5 which was uncooled, and the third for Mach 1.5, cooled. The chamber that the plasma would exit into was kept at a constant pressure of 2 kPa. The flowing gas being tested was either pure argon, or argon mixed with 3-5% hydrogen. Optical emission spectroscopy was used to measure electron density within the plasma. Using a Boltzmann plot of emitted transition temperature vs. intensity, an approximation of temperature was extracted. Figure 1.4 shows the axial distribution of pure argon with different nozzles taken at the center of the flow. The low and high approximations are shown as well as the temperature assuming local thermodynamic equilibrium. Note that the low temperature approximation changes only slightly when comparing the Mach 3 and Mach 1.5 nozzles [38]. The

study does not go into how accurate the Mach number is, but it is expected that the free stream temperature would drop as the Mach number increases.

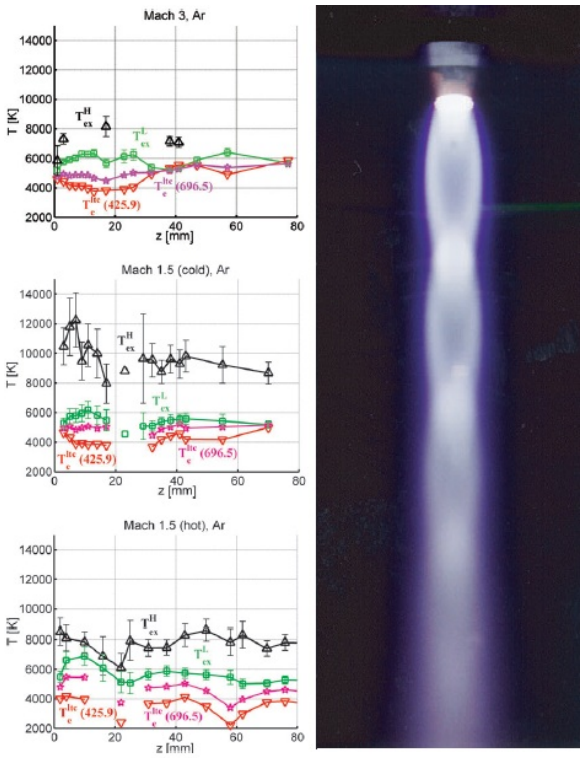

Figure 1.4: Axial temperature profiles of free stream plasma jet at the radial center of pure argon, taken at the Plasma Technology Research Centre, University of Sherbrooke [38]. High and low temperature compared with local thermodynamic equilibrium approximations are shown.

1.3 Velocity Gradient Effects

Other facilities have created supersonic plasma, but literature regarding the heat flux comparison between subsonic and supersonic plasma is scarce. The equations below derived from [21] and [20] give insight as to which components effect heat flux at the wall. The first equation is for the incompressible case, and the second shows the compressible case where subscripts s, and w are the stagnation point and wall

conditions.

$$\ddot{q_w} = 0.76(Pr)^{-0.6}(\rho_s\mu_s)^{0.5}(\beta)^{0.5}(h_e - h_w)$$

$$\ddot{q_w} = 0.76(Pr)^{-0.6}(\rho_s\mu_s)^{0.4}(\rho_w\mu_w)^{0.1}(\beta)^{0.5}(h_e - h_w)$$

Where Pr is the Prandtl number, ρ is density, μ is viscosity, and β is the velocity gradient given as $\beta = du/dx$. For the incompressible form, since $(\rho_s\mu_s)^{0.4}$ and $(\rho_w\mu_w)^{0.1}$ are the same for stagnation point and wall conditions, they are then lumped into one term. However, the ratio of the compressible (or supersonic) $(\rho_s\mu_s)^{0.4}(\rho_w\mu_w)^{0.1}$ terms to the subsonic incompressible $(\rho_s\mu_s)^{0.5}$ term is very close to unity. The Prandtl number ratio will also be very close to unity and we are left with the enthalpy and velocity gradient terms. $(h_e - h_w)$ should not change given that there is not a large entropy difference due to nozzle losses, therefore the equation only becomes a function of the velocity gradient [21].

1.4 Objective and Scope

The general objective of this research project was to advance the 30 KW ICP Torch Facility to achieve longer test times, higher heat flux, and to gain insight into the characteristics governing this facility. Different test methods are to be examined and executed to evaluate the facility's performance. The prior limitations of the injection system are also investigated due to heat induced failures. A new water cooled system is designed and tested in the facility, improving sustainability of the ICP torch. The three types of heat flux measurement devices are examined to converge to a trusted device, and supersonic nozzles are also designed and constructed in order to achieve higher heat fluxes, and expand the capabilities of UVM facility.

Chapter 2

ICP Facility Theory and Setup

2.1 Theory of Induction Plasma

Historically, induction heating was first used to heat treat different types of electrically conducting metals, and their application is still in use today. Depending on the application, induction heating can be a preferred way to provide heating because it is non-intrusive. The setup involves a power source capable of producing a large high frequency oscillating voltage. The voltage is carried to a copper coil which produces a varying magnetic and induced electric field. The material is placed within the coil which can have many different geometries to optimize and tailor heating locations.

Inductively coupled plasma torches for aerothermal heating applications uses a very similar setup. The largest difference being that the work piece is a conductive flowing gas. Typical main components of an ICP torch are a copper coil carrying a radio frequency (RF) current, and a quartz tube where a flowing gas is sent through, see figure 2.1(a). Though a quartz tube can be replaced with something

like Silicon Nitride, quartz is less expensive and works well in low powered facilities. Since a gas is much less conductive than a metal, the frequency and power must be altered to achieve a plasma discharge. Using Faraday's law, Lenz's law, and Ohm's Law a sustained plasma can be created given the proper setup.

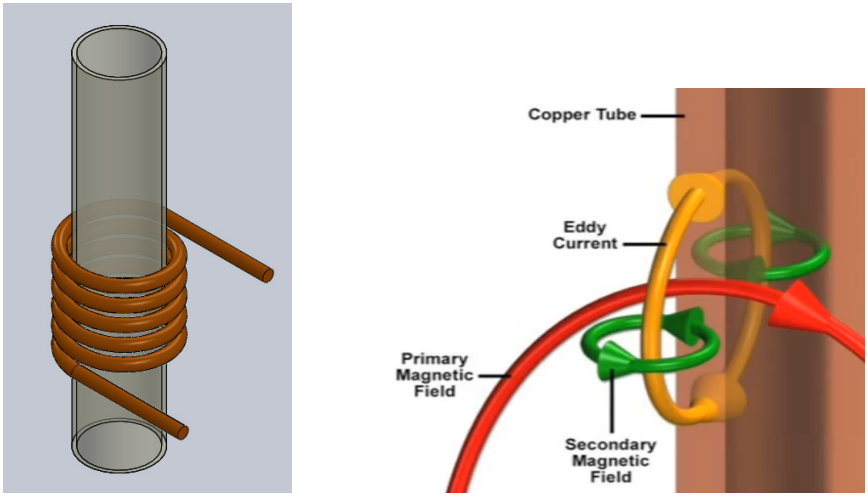

(a) Quartz tube with copper load coil.

(b) Lenz's law.

Figure 2.1: (a) Shows a typical coil and quartz tube. (b) A depiction of Lenz's law showing a primary magnetic field which induces an eddy current, which again induces a magnetic field and the pattern continues indefinitely [27].

Given a copper coil with an RF current running through it, a magnetic field is induced within the coil, as per Faraday's law. Figure 2.1(b) shows how the magnetic field also holds within it an electric field. This pattern of oscillating magnetic to electric field extends to the center of the coil radius with decreasing energy, following Lenz's law. A higher electric and magnetic field close to the inside of the coil cause a decrease in plane intensity from the edge of the coil to the center, which leaves the most intense part of the plasma closest to the coil. This distance is called the skin depth which will prove to be a design point later on. Since Lenz's law produces eddy currents in a conductive flowing gas, the gas must have a resistance.

Ohm's law states the when a current flows through a conductor, there must be some resistance which will induce heat. The larger the voltage applied, the larger the current, and the more heat is produced.

A typical RF circuit is shown in figure 2.2 where V, I, L, and R are the voltage, current, inductance, and resistance. The subscripts rf and p denote radio frequency and plasma. The equivalent resistance of a plasma can be estimated to some degree, although it is easier if an equivalent circuit is made as shown in figure 2.3.

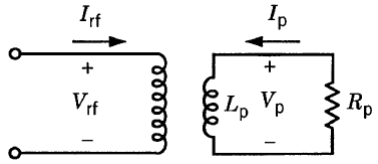

Figure 2.2: A typical RF circuit model of an ICP torch, where subscript p denotes plasma [25].

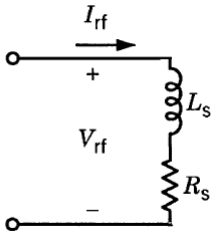

Figure 2.3: The equivalent RF circuit for ICP torches where the subscript s denotes system [25].

The equivalent resistance and the skin depth of the system are given in the equations below where N is the number of coil turns, r is the radius of the plasma, σ is the effective conductivity of the plasma, l is the length of the coil, μ_0 is the effective permeability, f is the frequency, and δ is the skin depth of the plasma. It is easier to think of the plasma ball as a cylindrical shell having thickness δ as in figure 2.4.

$$R_s = N^2 \frac{2\pi r}{\sigma l \delta} \qquad\qquad \delta = \sqrt{\frac{1}{\pi f \mu_0 \sigma}}$$

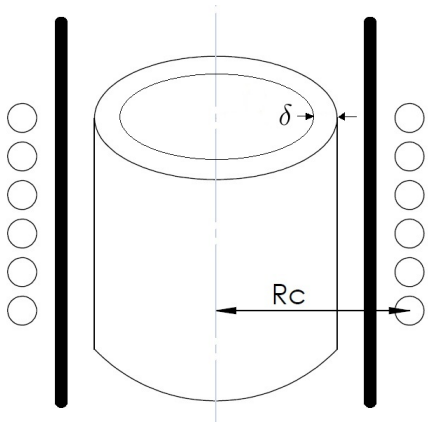

Figure 2.4: R_c represents the distance from the center to the outside of the coil and δ is the skin thickness.

2.2 Mechanical Design Considerations

Since the magnetic and electric field have the highest energy density closest to the inside of the coil, a design point is to have the flowing gas as close to the inside of the coil as possible. The power into the plasma is simply $P = \frac{1}{2} I_{rf}^2 R_s$ [25], which means that as the current goes down due to Lenz's law, the power into the plasma will diminish to the power squared, and thus the plasma will fade as well. Obviously the coil needs some space from the quartz tube to be cooled, leaving a small annular gap. Axially, the coil turns should be as close together as possible to raise the magnetic density, but spaced far enough away from one another to prevent arcing between turns. In order for a virgin flowing gas to have time to couple with the plasma, the gas needs to be slowed. This can be done mechanically a couple of ways. The first is to swirl the gas as it goes up the quartz tube which slows the gas and centrifugal force allows uncoupled gas to flow freely on the inside of the quartz tube. The other way is to create a recirculation zone where the gas can relax and effectively mock a very low velocity due to a recirculating vortex. This gives the

power supply time to couple to a small amount of gas, and the outer sheath gas that isn't slowing down convectively cools the inside of the quartz tube.

The gas injection system of the torch is arguably the most important subsystem, but other devices need to be in place for everything to work properly. ICP torches used for aerospace material testing are usually kept at low pressure to accurately recreate a reentry. Unfortunately, the power supply circuitry is limited to a finite pressure "envelope". In other words, an ICP torch cannot be operated at 0.7 kPa owing to too high of an energy density at the tube wall. Thus, with every circuit setup, there is a "comfort zone" for each plasma torch. Typically, a facility will have a vacuum pump capable of evacuating a chamber down to near vacuum, and mass flow controllers to regulate the flow of test mixture.

2.3 UVM ICP Torch Operation Setup

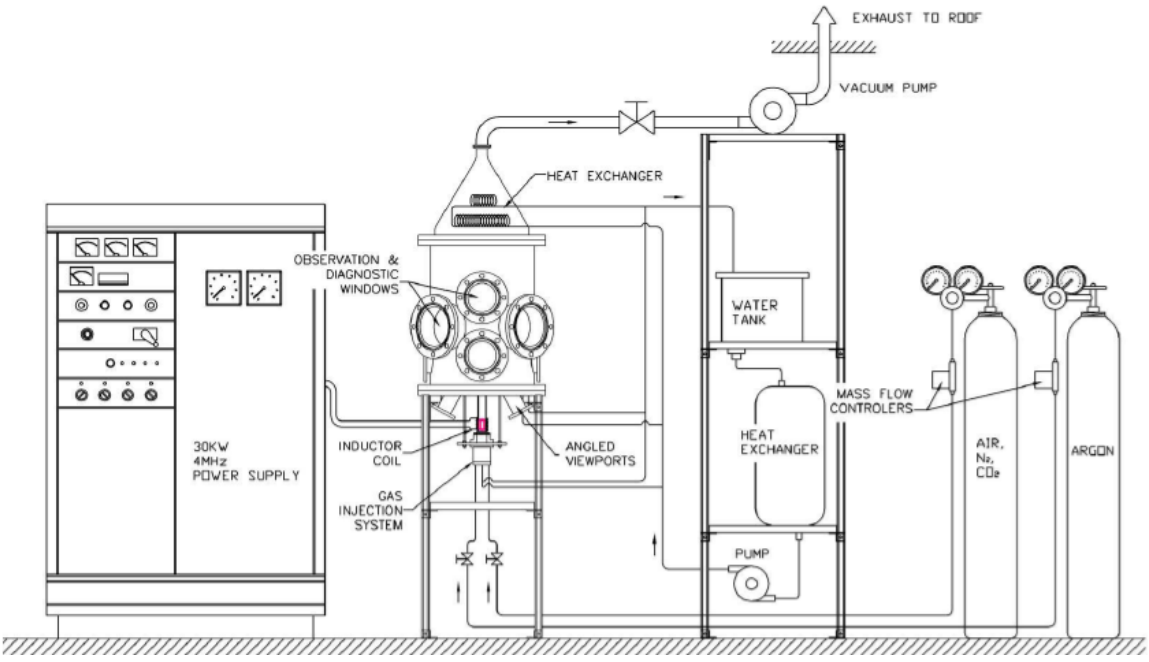

Figure 2.5: The overall layout of UVM ICP torch [35].

Figure 2.5 shows the entire layout of the facility. On the left is a 30 kW Lepel RF power supply. The gas injection system is shown in more detail in figure 2.6. On top of the injection system sits the test chamber where the material testing takes place. The exhaust gas exits to the vacuum pump which is capable of reducing the chamber pressure down to near vacuum. The circulating water and heat exchanger cools the entire facility and the power supply. The chamber is equipped with 4 large, and 2 small view ports to monitor and access the plasma flow.

2.3.1 Injection System

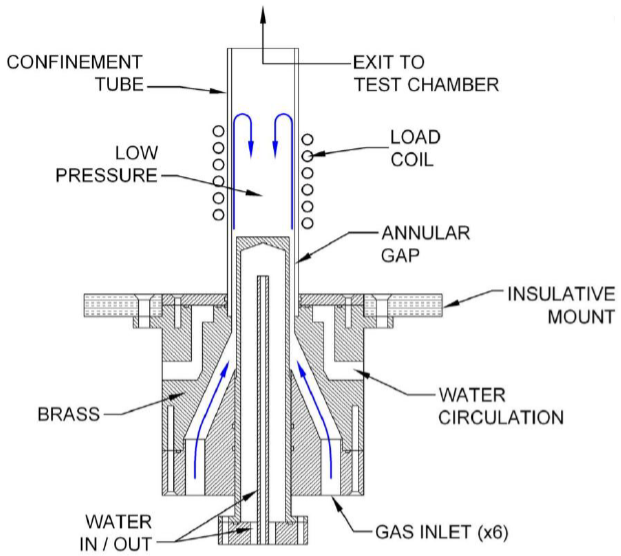

Figure 2.6: UVM's current gas injection system [35].

Figure 2.6 shows the gas injection system utilizing the recirculation method. Gas is injected into the bottom of the injector block and a cylindrical vortex is created allowing the gas to be coupled into a plasma. There is an insulative mount made from Ultem to make sure the coil does not arc to the grounded injector block. Water cooling is brought to the entire system, as well as the center brass insert which sits below the plasma ball.

2.3.2 Cooling System

Most components in the facility are water cooled by a recirculating pump with a heat exchanger. Water runs to the top of the chamber where the plasma is cooled via an array of heat exchangers. Two probes use concentric water cooling which are attached to flanges on the chamber. The power supply has its own water cooling loop, but uses the main heat exchanger in parallel with the torch.

2.3.3 Control System

The torch can be operated completely manually, but it is easier to use a LabVIEW program that controls the subsystems while logging data simultaneously. The mass flow can be adjusted with a slider, chamber pressure is controlled by a PID (Proportional Integral Derivative) control loop, and data are taken from several thermocouples to measure water temperatures. Warning lights appear when certain water temperatures an unsafe threshold. The power supply however is controlled manually because fine tuning of the circuit is required during testing. Although it is possible for the ICP torch to operate with only one person, safety protocol warrants at least two people.

2.3.4 Probe Testing Setup

The two test probes are concentrically water cooled, but both have an unfilled tube in the center as an auxiliary port. This is convenient when the back side of the test sample needs direct water cooling. The main difference between the retractable probe and gooseneck is mobility. The retractable probe has three degrees of freedom, and can move in the plasma during a test. Mobility is controlled by long threads on the retractable probe, whereas the gooseneck probe moves only to a

preset position. The gooseneck probe has one degree of freedom during testing, where it can only swing into the flow, but prior to testing, the gooseneck probe can be moved laterally. Typically the retractable probe is used to mount samples, and the gooseneck probe is used to mount heat flux probes. Generally the retractable probe will only move in and out of the flow, which is convenient when transitioning between start-up and test conditions, and occasionally the retractable probe will need to be moved axially to adjust height.

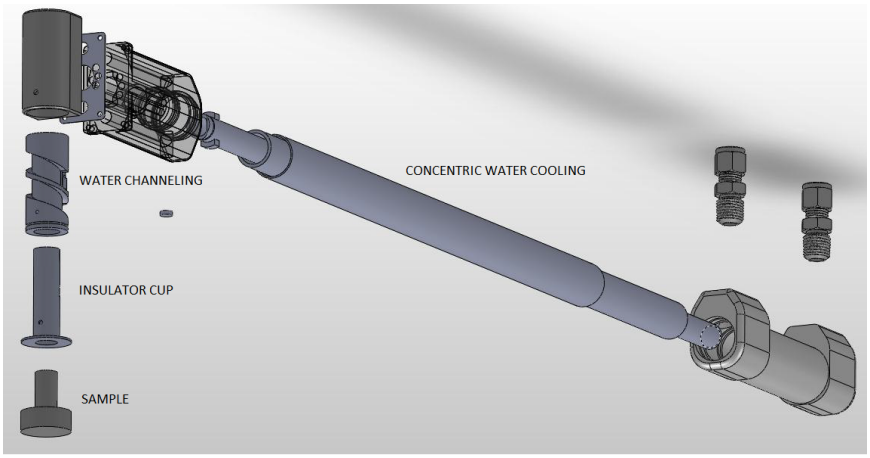

Figure 2.7: Retractable probe [41].

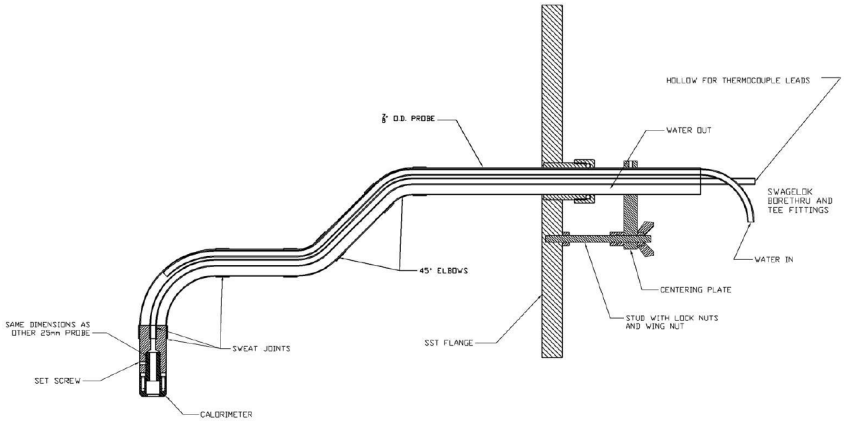

Figure 2.8: Gooseneck probe [35].

2.4 Plasma Torch Characteristics

Now that all of the major components have been presented, this section covers the main attributes of operating the ICP torch. Most measurements were done with the water cooled calorimeter which will be explained later in the "Heat Flux and Pressure Testing Methods" section. The water cooled calorimeter was chosen because even though it is not the most accurate, it can continuously take data in real time.

2.4.1 Start Up Procedure

The ICP torch takes about 2 minutes to come to a steady state test condition. When the power supply is shut off, it "remembers" what conditions it was turned off at. When turned on again, it will revert back to those conditions even if the power is lower since the power supply actively tries to match the test gas's electrical properties. This may seem like a drawback, but it increases the system's efficiency. Owing to this phenomena, when the torch is started it will sometimes have poor coupling and will need to be shut off and turned on again. Once the power supply is back to the proper start up conditions, the following procedure is followed (using $C0_2$ as the test gas), argon is only considered a start up gas, and not a test gas. The procedure has also been graphed in figure 2.9. Note that the procedure remains the same for different test gases.

UVM ICP torch Start Up Procedure

1. Chamber pressure is brought down to near vacuum (0-0.8 kPa)
2. 10 slm Argon gas is released to injection block
3. Power supply is turned on

4. Vacuum pump closed

5. 30 slm Argon gas

6. Power up to 20%

7. Set chamber pressure to desired pressure

8. 10 slm test gas

9. Power up to 25-30%

10. 40 slm test gas

11. Power up to 35 %

12. Argon down to 0 slm

13. Power up to desired range

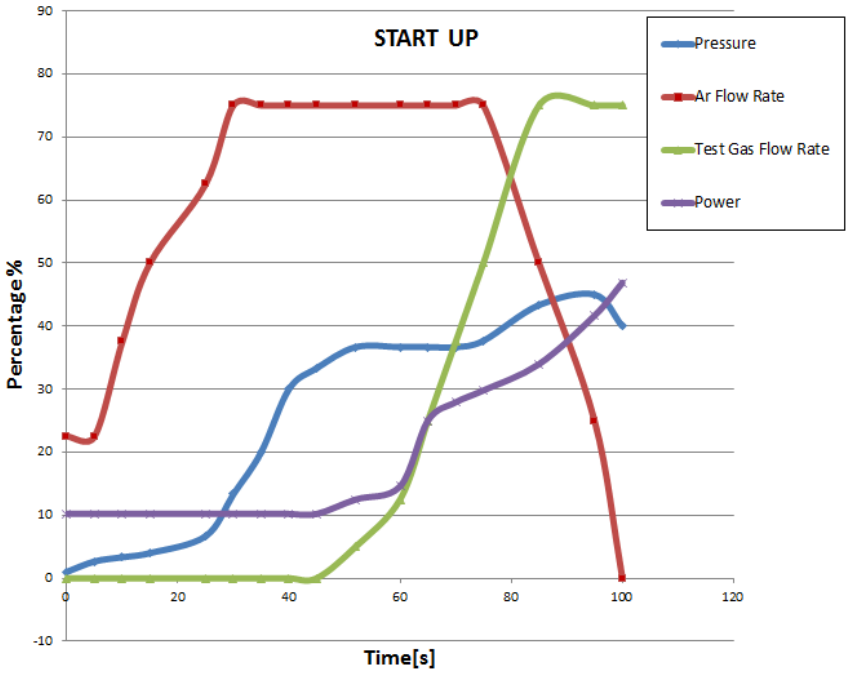

Figure 2.9: The UVM ICP start up graph.

2.4.2 Heat Flux vs. Power

Power is measured by the gages on the power supply, however they only display power input. Since the maximum output is 30 kW, the input readings are scaled down due to lossy components. The simple formula of $P = IV$ is used to calculate power where I is current and V is voltage. A Rogowski coil is typically used when measuring current, but the setup is risky with such a high oscillating voltage. Even though the scaling approximation is not totally accurate, it is a good approximation. Figure 2.10 shows the heat flux vs. ICP torch power for chamber pressures of 13, 20, and 26 kPa. The higher test pressures were tested at a higher power to avoid quartz tube failure. Owing to response time of the water cooled calorimeter, trailing heat flux is shown to increase when no more power is added, which can be seen clearly on the 27 kPa test.

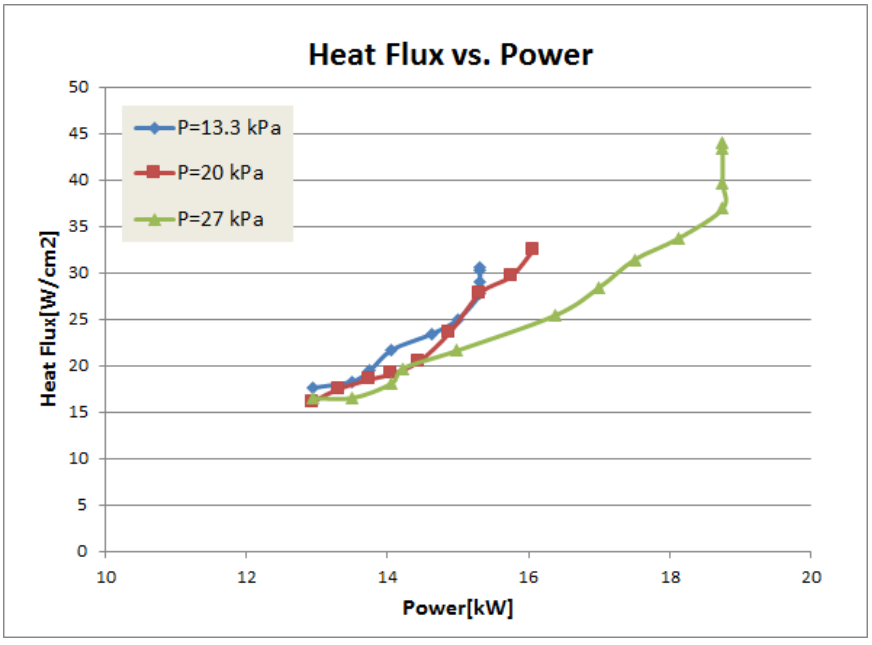

Figure 2.10: Heat flux vs. ICP torch power is shown while testing $C0_2$ at different chamber pressures.

The results show a fairly linear pattern as expected, but when the chamber pressure

is at 26 kPa, heat flux seems to go down. This could be due to the calorimeter's poor response time, the position of the center insert inside the injector block, or the probes position in the flow. Due to slight coil misalignments, sometimes the plasma will lean from side to side, causing the test probe to be slightly out of alignment.

2.4.3 Heat Flux vs. Probe Position

Again, CO_2 was used to test how the axial distance affects heat flux. The water cooled calorimeter was first placed at 14 cm above the exit of the quartz tube. It was moved down in increments of 6 mm until it reached the retractable probe's limit which is 8.25 cm. It should be noted that the probe's limit is a relative term because the probe was designed to take on attachments that could bring the distance down even lower.

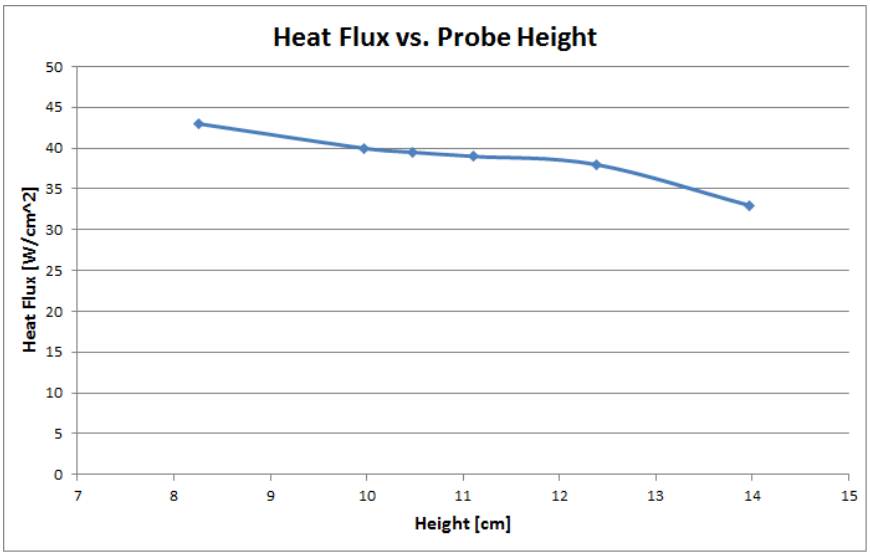

Figure 2.11: The ICP torch probe height vs. heat flux at a constant pressure and flow rate of 21 kPa and 26 slm.

2.4.4 Heat Flux vs. Probe Radial Distance

Nearly the same conditions were used to test the heat flux radial dependences, the only difference being that pressure was held constant at 24 kPa. As mentioned earlier, the plasma column can have a slight lean which is what we see in figure 2.12 from asymmetry, and in figure 2.13. Had the water cooled calorimeter been capable of only measuring the center of the probe at the stagnation point, the results would more likely show a parabolic distribution. The calorimeter takes an average reading of the total heat flux that reaches its surface.

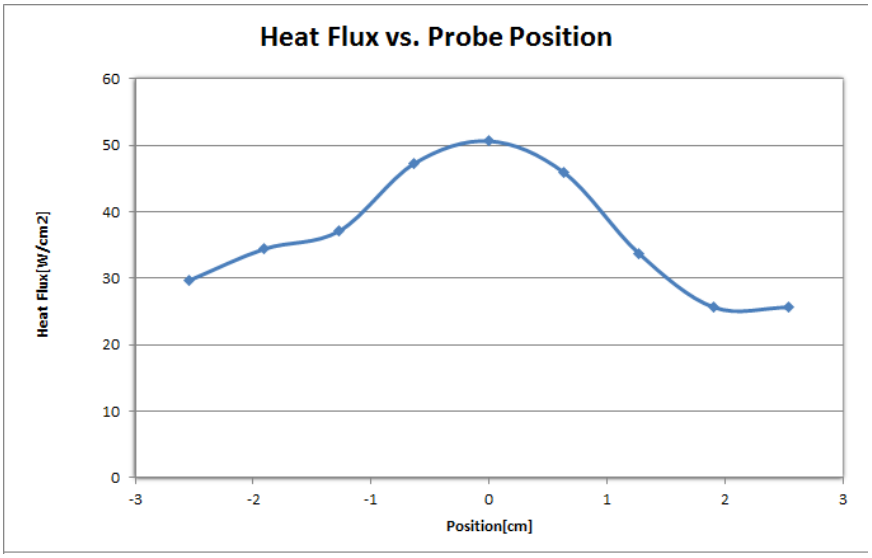

Figure 2.12: The heat flux vs. ICP torch radial probe position at constant pressure and flow rate of 24 kPa and 26 slm CO_2.

2.4.5 Static Pressure Range

It is possible for the ICP torch to run at a pressure near vacuum, but not for a long duration. On the higher pressure scale however, the torch will extinguish near 29 kPa. The plasma flow tends to be turbulent at 13 kPa, and transition around 20 kPa as seen in figure 2.13.

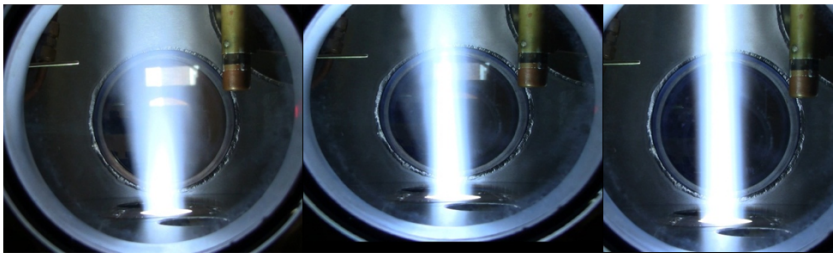

Figure 2.13: The low end of steady state operation is near 13 kPa, transitions at 17 kPa, and extinguishes near 29 kPa. Shown for 26 slm CO_2.

Figure 2.13 shows turbulence at 13 kPa, transition 17 kpa, and a laminar flow at 21 kPa. Near 27 kPa, the density becomes too high for the power supply to couple with the gas. Tekna Plamsa however, has designed their power supply to run at atmospheric conditions. Having the ability to couple a gas from near vacuum to atmospheric pressure would greatly extend the test conditions to allow fuller flight simulation capability. However, being able to run the ICP at low pressures would mean certain mechanical challenges would need to be overcome. As pressure decreases, the sheath gas that cools the quartz tube gets thinner, and less dense, meaning that the convection coefficient will rapidly decrease. If the torch is exposed to these conditions for too long, the quartz tube will exceed its limit temperature and likely form a hole next to the coil.

High temperature o-rings are used to seal the top of the brass insert to the quartz tube and these slowly melt during regular operation, and typically need to be changed after ≈ 5 hours. When a low pressure or high enthalpy simulation is needed, it vastly decreases the life of the o-rings and quartz tube. The torch can operate with the o-rings partially failed, but this allows atmospheric air to enter into the system. In order to minimize maintenance and unexpected failures, either a water cooled system needed to be built, or the main failure points needed to be

improved. Typically ICP torches that are over 30 kW use either a water cooled quartz system, or use Silicon Nitride in place of the quartz tube. Some systems embed the coil into the Silicon Nitride which eliminates the need for o-rings. These systems are not only costly, but difficult to manufacture. For our facility, our first choice was to develop a water cooled injection system.

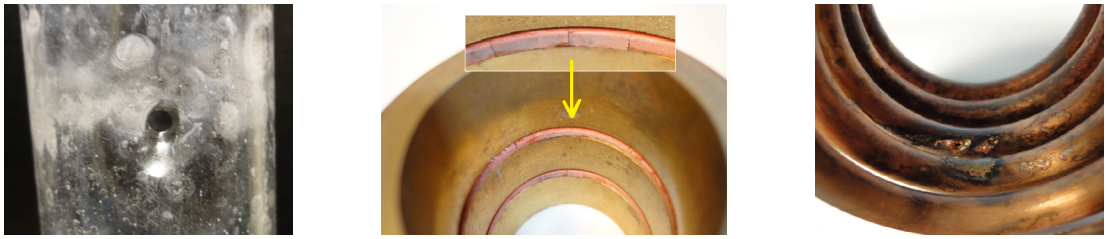

(a) Quartz tube failure (b) O-ring failure (c) Coil failure

Figure 2.14: Typical injection system failures due to localized high heat. (a) hole in the quartz tube due to excessive heating, (b) o-ring failure over a prolonged exposure, and (c) arcing between coils due gap being too small, or excessive heat.

2.5 Water Cooled Injection System

The overall goals of the water cooled injection system were: 1) to be able to push the power supply to its maximum power producing the highest heat fluxes, and 2) to run at lower pressures without a quartz tube failure. Test times were limited to about 20 minutes, whereas this system also looked to expand to 60 minutes if need be. ICP torches typically use a water cooled enclosure to cool the quartz tube and coil. Some systems have the coil submerged in the water, while others are large enough to have two concentric tubes, one for the inner gas flow confinement tube and the other for water cooling with the quartz tube on the outside of both. The VKI Plasmatron makes use of the double tube system, whereas the PKW-3 (shown in figure 4.7) uses a coil embedded into a ceramic shell and a quartz tube in the center.

2.5.1 Design

Due to the small scale of the UVM facility, a double quartz tube system was not a viable solution. The entire assembly needed to fit into an area nearly 30 by 15 by 15 centimeters. Sealing the system was also a challenge because on the cooling side of many components there is water flowing at 140 kpa, whereas the other side needed to maintain a pressure near vacuum. Since the test chamber is grounded, the system also needed to be electrically isolated from both the lower injector block and the upper chamber. Taking into account all of these considerations, a system was created that allowed cooling water to reach the top brass insert, with a lower compartment for cooling the coil and quartz tube as seen in figure 2.15.

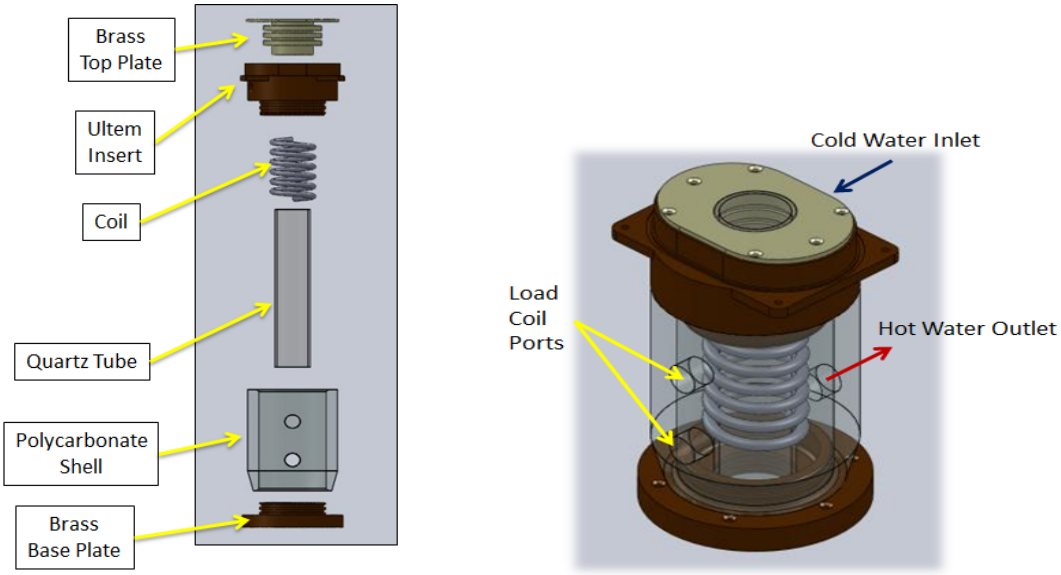

(a) Exploded view (b) Collapsed view

Figure 2.15: The water cooled injection assembly showing the components on the left and the in/out ports on the right.

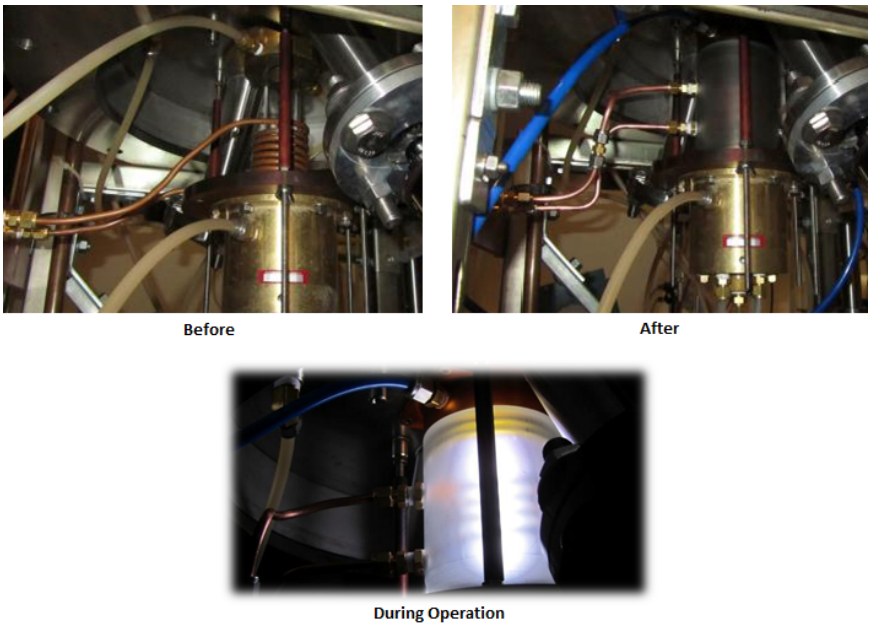

Figure 2.16: Water cooled system prior to and after installation shown on top, and during operation shown on bottom.

After installation, the system successfully supported the large pressure differential allowing the chamber to be evacuated to 0.03 kPa. Distilled water from the power supply was used to cool the assembly by using the top as the input and the bottom as the outlet. However, after the installation arcing appeared from the brass top plate to the grounded stainless steel chamber shown in figure 2.17. Only an argon plasma could be created because the torch would extinguish if a test gas was added. Two hypotheses were taken into consideration; either the coil that was in direct contact with the water was carrying the charge to the conductive brass top plate, or the water was being charged due to induction. Both hypotheses suggested that the water was charged which was transfered to the top brass plate, and then to the stainless steel. This did occur prior to the new installation, but was manageable and relatively weak. A small gap between the brass top plate and the chamber was used as an electric insulator. Ultem was also used for this same reason because it has

very good heat and electric insulative properties. Removing the ground wire from the chamber was an option, but risky due to sensitive instruments attached to it, and not to mention the safety risk of physically touching the chamber.

Figure 2.17: Arcing during a pure argon test shown on the left, and nitrogen-argon mixture on the right.

2.5.2 Modifications

Efforts were made to minimize the arcing problem by isolating the charged water from the chamber. The copper coil was wrapped five times in Teflon heat shrink tubing, which helped but melted shortly after testing. A Teflon insert was machined to act as a barrier between the Ultem insert, and the polycarbonate shell. This acted to create two zones of cooling. A thicker, more rugged 1 mm thick Teflon tube was also added to prevent direct conduction into the water. All of the mentioned modifications did have a positive impact on the arcing problem, but some arcing still remained. Compressed air was introduced into the compartment that houses the coil, as an alternative to water. This modification proved to be a success as test gases could be added, however the torch was unstable and would sporadically extinguish. After investigation, the compressed air used to convectively cool the quartz tube was found to have a fair amount of moisture in it, which made the coil

arc between turns. If a vapor trap had been used upstream of the compressed air zone, the coil arcing may not have persisted. All of the modifications can be seen in figure 2.18. In summary, the modifications helped reduce arcing, but this wasn't the only issue. Even when arcing was kept to a minimum, the power supply output was extremely high, yet the resulting plasma had low output. This meant that the efficiency using the water cooled system was poor compared to the prior natural convection system. Preoccupation with further modifications can lead to forgetting of the overall goal; in our case to increase heat flux and create a more sustainable system.

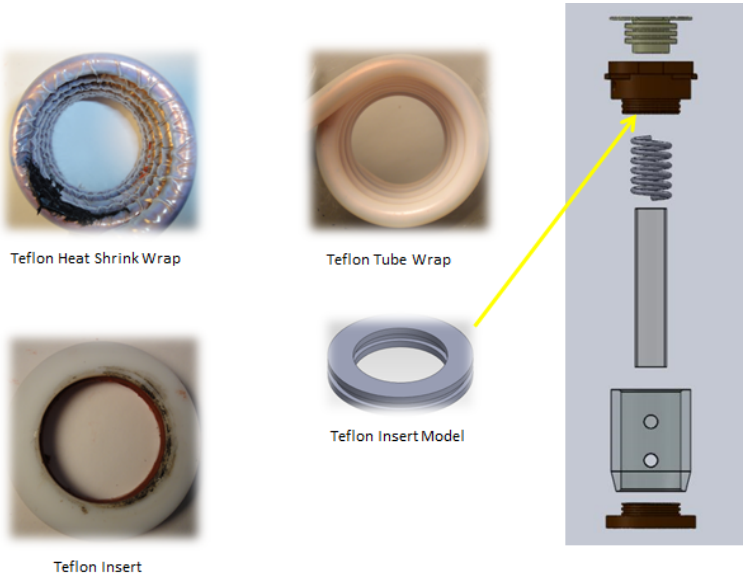

Figure 2.18: Modifications made to the eliminate arcing to the chamber.

The attention then moved to the weakest point in the sealing system. Recall that high temperature o-rings are used between the quartz tube and brass insert to seal ambient air from entering the system. Unfortunately, these o-rings will melt at nearly 500 °C. Cotronics corporation produces sealants that are able to withstand temperatures of 1360 °C, but the sealant is a porous material. The gap between the quartz tube and the brass top plate is only 0.025 mm and the sealant was placed

between and around the o-rings and installed as seen in figure 2.19. The sealant needed to be able to uniformly expand upon heating so the quartz tube, or sealant would not crack during operation. Since the quartz tube has a low linear expansion coefficient, and brass is high, the sealant needed to be in the middle. The brass top plate is water cooled, which maintains the temperature around 100 °C, so it would not expand very much. The sealant 940-LE was chosen because of its "low expansion" properties. This modification proved to be reliable as it is currently used in the UVM ICP facility. Even though the o-rings have partially failed, the fully evacuated pressure still remains near 0.1 kPa due to the sealant.

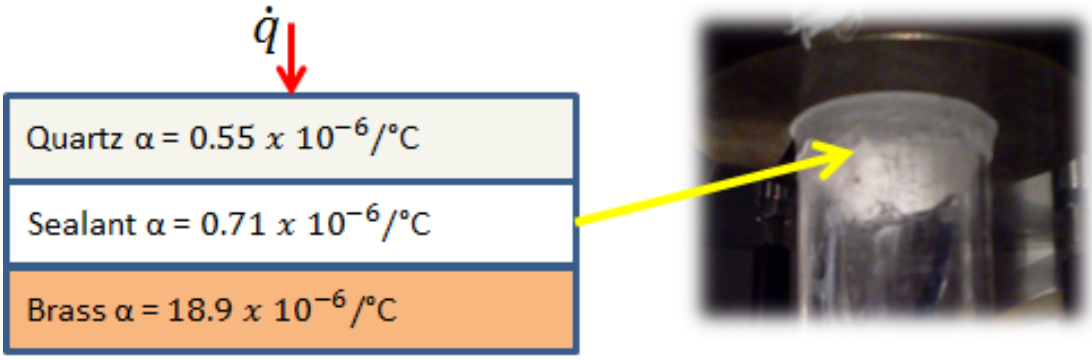

Figure 2.19: A sealant added to the surrounding area of the o-rings.

Active cooling of the quartz tube is still a challenge remaining, but a fan has been installed in a closed area surrounding the quartz tube and components to boost air cooling and this appears to work. A vortex air cooling system has been proposed, but it is not needed at the moment because the heat fluxes achieved are suitable for materials being tested. However, this will be short lived and the facility will need to push the limits of the power supply, and the vortex cooling system will likely be needed. Three columns of five air jets 120 °apart driven by water free compressed air should be sufficient for a forced vortex cooling system. Figure 2.20 illustrates

this design.

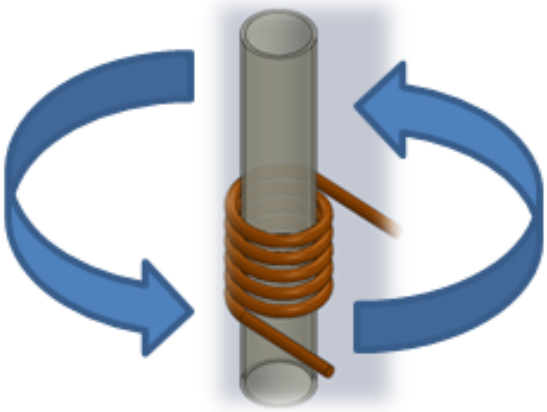

Figure 2.20: Proposed quartz tube cooling vortex.

Chapter 3

Heat Flux and Pressure Testing Methods

Heat flux and pressure measurements are acquired from the gooseneck probe system in the facility. Having two probes is convenient because one can be used to test pressure or heat flux, while the other is used for material testing. When a material is being tested, it is useful to get a corresponding heat flux to document test conditions. The retractable probe is generally used to hold the material being tested, while the gooseneck probe is extracts a heat flux value. The geometry of the sample is the same as the geometry of the heat flux probe, allowing for consistent velocity gradient effects.

3.1 Heat Flux

Heat flux is the amount of heat energy transfered per unit area to a given surface. W/cm^2 are commonly used units referring to heat flux of reentry vehicles. As mentioned in chapter 1, the equation describing heat flux to the surface of a vehicle

is a function of many different parameters, but it also applies to heat flux calorimeters with known characteristics. Depending on the test conditions, the ICP facility can provide strong convection and possibly significant radiation to the surface of the calorimeter. The slug, water cooled, and Gardon gage calorimeters are more commonly used in high enthalpy testing facilities. They each have their limitations, but can be fairly accurate when used correctly.

3.1.1 Slug Calorimeter

A slug calorimeter uses a thermal mass (usually copper) to measure heat flux. The setup generally consists of a cylindrical copper slug with the front face exposed, an air gap or insulator on the side, and a thermocouple mounted on the center on the back face. A Teflon tube is used to slide over the side wall creating a thermal barrier from the housing, shown in figure 3.1. This calorimeter is mounted on the gooseneck probe and is generally used before and after material testing.

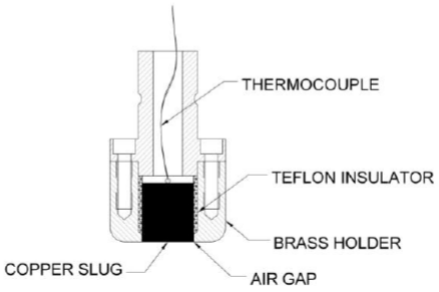

Figure 3.1: Slug calorimeter schematic [35].

$$\ddot{q} = C_p \frac{m}{A} \frac{\Delta T}{\Delta t} = C_p \rho l \frac{\Delta T}{\Delta \tau} \tag{6}$$

Where $\ddot{q}$ is the measured calorimeter heat flux, ρ is the density, C_p is the heat capacity of the slug, l is the distance from the front face to the back face where the thermocouple is mounted, ΔT is the temperature change during exposure, $\Delta\tau$ is the time during exposure corresponding to ΔT, m is the mass of the slug, and A is the cross sectional area of the slug exposed.

The equation above is used for the ideal case, but there are losses from the readings given by the slug. After the front face of the slug calorimeter has been tested, there will be a consistent small drop in temperature, due to imperfect insulation. If this temperature loss due to conduction from the holder is seen after exposure, then it must be happening during exposure as well. Taking the loss into consideration, the new equation becomes,

$$\ddot{q} = \frac{mC_p}{A}\left(\left(\frac{\Delta T}{\Delta \tau}\right)_{Expose} + \left(\frac{\Delta T}{\Delta \tau}\right)_{Loss}\right)$$

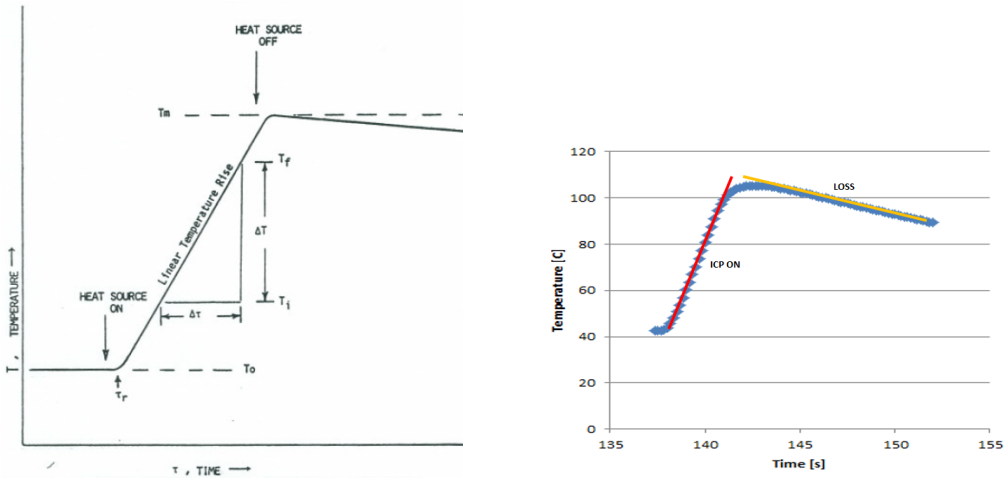

(a) Slug calorimeter response.

(b) ICP slug calorimeter data.

Figure 3.2: (a) slug calorimeter data during heat exposure and cool down, (b) typical data from UVM ICP torch [6].

As seen in figure 3.2(b), the conduction loss does play an important role in finding the total heat flux. Typical conduction losses are near 2-5% of the total heating

level in the UVM ICP facility. ASTM recommends this not exceed more than 5%. The slug calorimeter does have a response time that is dictated by the slug's time of heat transfer, so finding the steepest average slope is often the best choice to alleviate response delays. Since copper is generally considered to be a fully catalytic material, it's also important to keep the front face polished before exposure. The uncertainty of the slug calorimeter is generally around 5% mostly due to measured temperature uncertainty conduction loss. In general, it has a low susceptibility to electrical noise in ICP facilities, making it a dependable device.

3.1.2 Water Cooled Calorimeter

A water cooled calorimeter uses the temperature differential between incoming cooling and hot exit water to determine heat flux. It is a simple and robust way to determine heat flux, but can be difficult to use with high accuracy. The apparatus typically has cold water flowing onto the back of the testing surface to remain cool, and an insulator on the exposed side wall to preclude unwanted convective side heating. This method is often preferred because real time heat flux measurements can be gathered and exposure time is virtually unlimited. The setup is shown in figure 3.3.

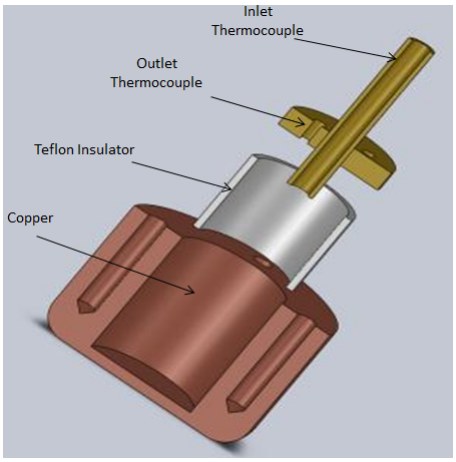

Figure 3.3: Model of the water cooled calorimeter.

The UVM water cooled calorimeter uses the same outer edge geometry, and Teflon insulation technique as the slug calorimeter. The inlet tube is placed concentrically to let water flow on the back side evenly, and then exit through a barrier with five evenly spaced holes. Thermocouples measure inlet and exit water temperature just upstream of the tube exit and at the water barrier, respectively. The equation below is used to calculate the steady state heat flux.

$$\ddot{q} = \frac{\dot{m}C_p}{A}(T_{Exit} - T_{Inlet})$$

Where $\dot{m}$ is the mass flow rate of water, C_p is the specific heat capacity of water, A is the exposed area, and T is temperature of the inlet and exit water. Mass flow rate and insulation have a large impact on accuracy when designing a water cooled calorimeter. There needs to be enough of a flow rate to adequately cool the unit while avoiding saturation of the temperature readings, and flash boiling, yet low enough to provide a good temperature differential. Since the unit is not transparent, it is difficult to know if flash boiling is taking place. The concern would be energy consumption during a phase change is unaccounted for in the calculation. A good design will keep the outlet water temperature well below boiling, but still

have a good differential to work with. If the differential is too small, then accuracy is at the mercy of the thermocouple readings. Insulating the side walls from convection is also important. The UVM calorimeter outer geometry was configured to match material test samples, which owing to the scale of the UVM facility, test sample and calorimeter diameters are currently limited to a 25 mm diameter, making it difficult to design and machine complex parts. The blueprint of the water cooled calorimeter can be seen in the Appendix. Unfortunately, the UVM water cooled calorimeter falls subject to heat transfered from the side wall to the measurement area of the calorimeter. In larger scale facilities, a double water cooled design is often used, as shown in figure 3.4, where a insulative bushing provides a barrier between water cooling zones.

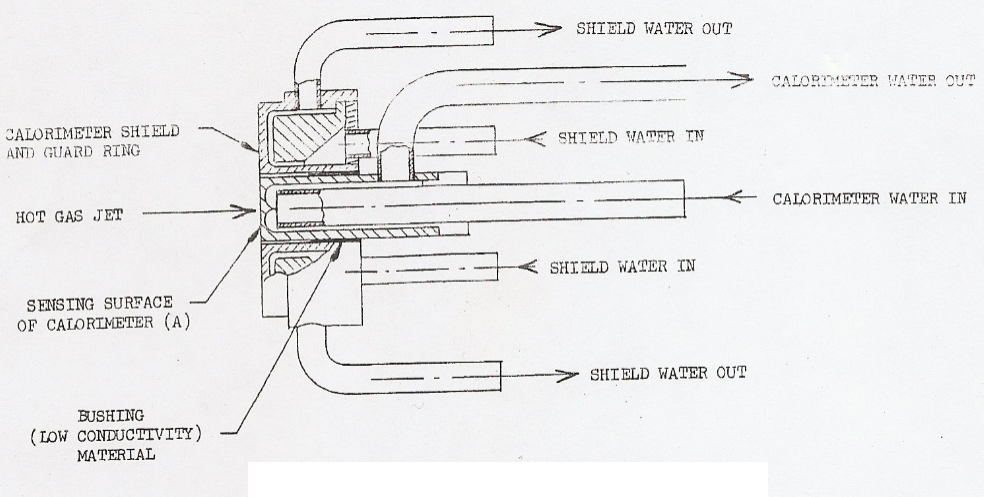

Figure 3.4: Schematic of a water cooled calorimeter with side wall insulation. [5]

Since the UVM water cooled calorimeter allowed heating from the side wall, it needed to be calibrated with another calorimeter. The slug was chosen because of reliability, but uncertainty of the water cooled unit goes up. We estimate that our slug calorimeter has an uncertainty of $\pm 5\%$. The water cooled calorimeter uncertainty included with the slug calorimeter calibration is estimated to be $\pm$ 10%.

Electrical noise is also an issue with the water cooled calorimeter because ionized gases impinge on the surface of the ungrounded probe, transferring a charge into the flowing water. Susceptibility to noise is a function of thermocouple proximity to the front face of the probe head, the power input, and the plasma gas being tested. We have found that if the thermocouples are placed far enough away from the probe head, noise is reduced. There is a consequence however, because error goes up the with the distance thermocouples are set away from the front face. Heat can also be transfered from the outer cooling tube into the inner auxiliary line.

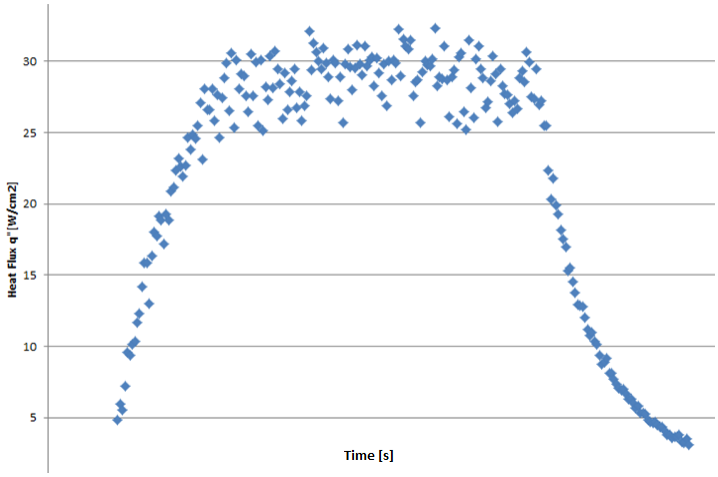

Figure 3.5: Water cooled calorimeter data noise.

Although the accuracy is poor, the water cooled calorimeter is still useful for visualizing plasma heating trends due to the its ability to stay in the plasma for long times. This calorimeter was used to find the characteristics of the UVM ICP torch in the previous chapter.

3.1.3 Gardon Gage

A Gardon gage is another commonly used calorimeter in high enthalpy flows. The setup consists of a thin constantan foil wrapped over a copper heat sink. The back

side of the foil is taken as an insulator. A copper wire is attached to the foil center on the back side and another wire is attached to the copper heat sink on the radius. The two thermocouples form a junction where temperature can be extracted. The proportion of heat flux to voltage difference is approximately linear. The copper heat sink must be cooled if the enthalpy is too high, or exposure time is too long. Figure 3.6 shows a typical layout of the Gardon Gage.

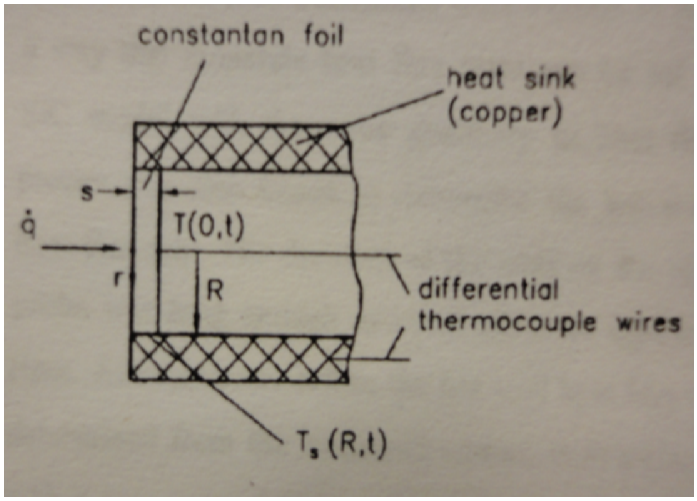

Figure 3.6: A schematic of the Gardon gage where s is the foil thickness, R is the radius, and T is temperature.

Gardon gages rely on a uniform parabolic temperature profile where the center has the highest temperature, and the edge has the smallest. For this reason, a good heat sink is needed on the outer perimeter of the gage. The equation describing the gage response to heating is shown below.

$$\ddot{q} = \frac{4sk}{R^2}\Delta T$$

Where s is the foil thickness, k is foil thermal conductivity, R is the radius of the foil from the center to the heat sink, and ΔT the temperature differential. Gardon gages are calibrated using radiative heating, while ICP and Arc-Jet facilities produce both radiative and convective flow. The two thermocouple leads measure

an electrical resistance that is a function of the foil's temperature integrated over the radius. Accuracy increases when foil thickness decreases and radius increases.

The UVM Gardon gage was made by Vatell Corporation with a quoted uncertainty of ±3 % and repeatability of ±1 %, but Vatell calibrates their devices in a pure radiation environment. Corrections can be made allowing testing in radiation and convection environment given in [8]. However, since shear flow is very minimal at the stagnation point, the resulting measured heat flux should be accurate in an ICP facility. In the UVM facility we estimate ours to be nearly 20 to 25 % based on recent measurements, which could be due to the non-catalytic surface. Gardon gages are also subject to noisy data, which can be even worse than the water cooled calorimeter. If a good water cooled Gardon gage was calibrated for convective flows, it would be capable of measuring heat flux in real time continuously.

3.2 Pitot Tube Testing

Velocity measurements can be made in ICP facilities using a Pitot tube which stagnates the flow transforming velocity into a higher pressure. The UVM ICP torch typically operates subsonically at a Mach number near 0.1, where the Bernoulli equation can be used to find velocity. A differential manometer designed for small pressure changes uses a Pitot tube of ⌀6 mm, and a static pressure tap in the side of the chamber to find the dynamic pressure. The commonly used equation below shows how velocity can be calculated.

$$v_\infty = \sqrt{\frac{2(P_0 - P)}{\rho}} = \sqrt{\frac{2\Delta P_{Dyn}}{\rho_\infty}}$$

Where v_∞ is the stream velocity, P_0, P and P_{Dyn} are total, static, dynamic pressure, and ρ_∞ is free stream density. This equation holds true for Mach numbers of less

than 0.3. For higher Mach numbers, compressibility must be taken into account since density is no longer constant. The equation below describes the ratio of total to static pressure. Generic pitot tubes usually have both a total pressure port facing the flow, and a static port normal to the flow on the side of the probe, whereas in our case we are assuming the static chamber pressure takes the place of the pitot static pressure tap.

$$\frac{P_0}{P} = \left(1 + \frac{\gamma - 1}{2} M_2\right)^{\frac{\gamma}{\gamma - 1}}$$

$$M^2 = \frac{2}{\gamma - 1}\left[\left(\frac{P_0}{P}\right)^{\frac{\gamma - 1}{\gamma}} - 1\right] \qquad [4]$$

In the above equation, γ is the ratio of specific heats and M is the Mach number. This equation works for $0.3 < M < 1$, but when the Mach number increases above unity, a bow shock wave will form in front of the pitot tube and the pressure reading will be not be the same ahead of the shock wave. To correct for this, we use the following equation.

$$\frac{P_{02}}{P_1} = \frac{P_{02}}{P_2}\frac{P_2}{P_1} = \left(\frac{(\gamma + 1)^2 M_1^2}{4\gamma M_1^2 - 2(\gamma - 1)}\right)^{\frac{\gamma}{\gamma - 1}} \left(\frac{1 - \gamma + 2\gamma M_1^2}{\gamma + 1}\right)$$

The Mach number can be solved for using a root finder where subscripts 1 and 2 denote before and after the shock wave. However, subsonic ICP facilities produce a flow where the Reynold's number (equation shown below) plays an important role.

$$Re = \frac{\rho v L}{\mu}$$

Where ρ is density, v is velocity, L is the length scale used, and μ is the dynamic viscosity of the flowing gas. Temperature and pressure both affect viscosity, but pressure is minimal compared with temperature. Viscosity can be estimated using

either the power law or the Sutherland law [42] as,

$$\frac{\mu}{\mu_0} = \left(\frac{T}{T_0}\right)^n$$

$$\frac{\mu}{\mu_0} = \frac{(T/T_0)^{3/2}(T_0 + S)}{T + S}$$

Where μ_0 and T_0 are known reference dynamic viscosity and temperature, and $S \approx 110K$ and $n \approx 0.7$ (from reference 26 in [42]). If density is assumed to follow the ideal gas law, and assuming a partially dissociated gas, the Reynold's number can be calculated with an estimation of velocity. The length scale is generally the diameter of the measurement orifice taken at the pitot tube head.

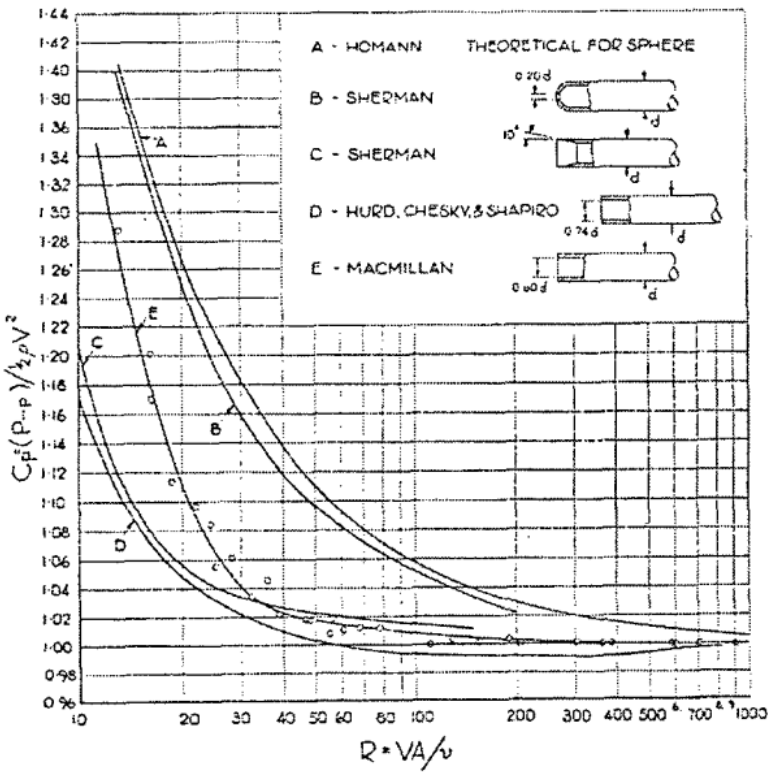

Figure 3.7: Graph of pressure coefficient vs. Reynold's number for different pitot tube inlet geometries [11].

The reason for a good estimate of the Reynold's number is the affect it has on pitot tubes. Considering the Reynold's number equation, density is low due to low

pressure and high temperature, the diameter (L) in a pitot tube is quite small, and owing to temperature increase, viscosity increases as well. The only factor that increases the Reynolds number here is velocity. Low Reynold's number flows have affects on pitot tubes below $Re = 1000$, but are negligible until $Re \approx 100$. Subsonic flows are subject to this effect because of their low velocity. To characterize the viscosity effects, the coefficient of pressure, C_p is commonly used.

$$C_p = \frac{P_{pitot} - P}{\frac{1}{2}\rho v^2}$$

Where P_{pitot} is the measured pitot pressure, and again P is the static pressure, ρ is density, and v is velocity. In a subsonic high Reynolds number flow, this equation would be unity. When the Reynold's number drops below 100, the value of C_P starts going up as seen in figure 3.7.

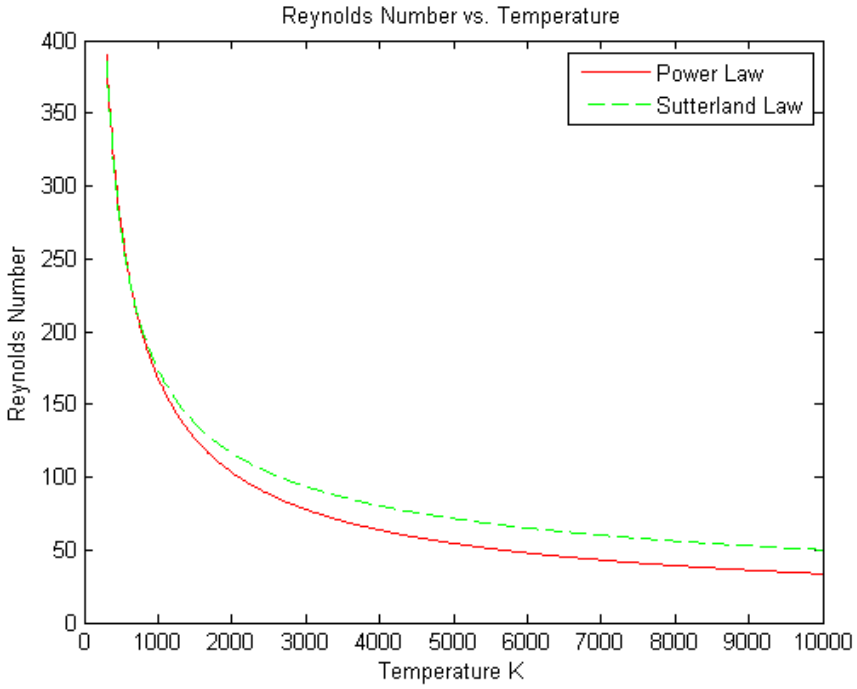

Figure 3.8: Estimation of Reynold's number in the UVM ICP facility using the characteristic length at the pitot tube inlet diameter.

From chapter 4, we see that the UVM subsonic velocity during a pure air test at 21

kPa is estimated to be 200 m/s using the Bernoulli equation via pitot tube (Mach number is estimated to be 0.15). Assuming a free stream temperature of 5000K, a pressure of 21 kPa, 5 species pure air, NASA's CEA program can be used to determine parameters such as density, molar mass mixture, specific gas constant, sonic speed, and many others if need be. With these parameters and the pitot tube diameter (6 mm) as the characteristic length scale, the Reynold's number is around 50. Figure 3.8 shows how Re_D varies for different stream temperatures using the power law and Sutherland law for viscosity. If we use the inside quartz tube diameter (36 mm) as the characteristic length, the Reynold's number is near 300. Since we are interested in the pitot tube, a Reynold's of 50 certainly falls in the low range. A correction factor is given by Homann as seen below.

$$P_0 = P_{Pitot} - \frac{1}{2}\rho v^2 (C_p(Re) - 1)$$
$$C_p = 1 + \frac{6}{Re + 0.455 Re^{\frac{1}{2}}} \quad [11]$$

Given the UVM ICP estimate of Reynolds number to be 50, from figure 3.7, the Homann solution provides a pressure coefficient of 1.10. If we adjust for the Homann relation, then the velocity gets reduced by 5 % to 190 m/s, which is a small difference. However, the line plotted by MacMillan shows that the coefficient of pressure is almost unity at a Reynolds number near 50, which corresponds to the UVM geometry. This being the case, according to reference 8 in [11], the existing correlation should hold true. For supersonic cases, viscosity does not play as much of a role because of the large value of v.

The pitot tube yaw angle can also play an important role in uncertainty. However,

if the angle is kept within 10°, the error will be less than 5% as seen in figure 3.9. That being said, the differential and static manometers used are fairly accurate (0.3% of reading) giving an overall estimate of 10% uncertainty.

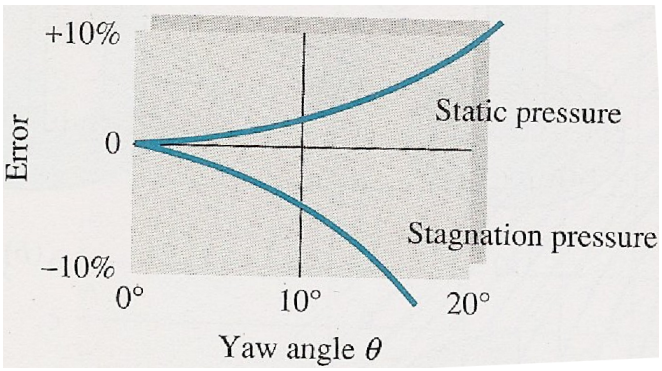

Figure 3.9: Pitot tube error from yaw angle [42].

Obviously estimates need to be made concerning uncertainty, but the traditional analysis cannot always be used because some factors are simply unknown. Therefore, uncertainty can only be estimated from literature and by confidence of what factors are more dominant in measurements. Experience and repetition play a large roll in understanding the uncertainty of these devices.

Chapter 4

Nozzle Design

The goal of designing a supersonic nozzle is to increase measured heat flux and plasma velocity. The subsonic system uses the full quartz tube inside diameter of 36 mm for the jet. When the diameter is reduced, velocity will rise which lowers temperature to conserve energy. The overall effects need to be investigated to determine the outcome for heat flux. To do so, existing supersonic ICP designs were taken into consideration along with an iterative nozzle design approach.

4.1 Preliminary Considerations

Our ICP facility operates within an envelope dictated by downstream pressure, mass flow rate, ICP electrical circuit configuration, and cooling elements. It is difficult to make an exact replica of a pre-existing nozzle design because other ICP facilities vary largely in their characteristics, and nozzles are tailored to their facility. Designing a nozzle by theory alone can be a good starting point, but since most of the parameters are not well known, this approach gets complicated quickly. For example, when the power supply is on and current is running through the load

coil, a plasma is formed in the flowing gas, but the percentage of the gas that is being ionized or turned into a plasma is much less than 100 %. Since pressure is a function of coupling efficiency, the pressure in the induction zone is not well-known. CFD can also be a good preliminary tool to begin the process, but it is a project of itself since most generic CFD programs cannot compute either the induction power input to the gas or the corresponding fluid properties. Given these constraints, a multistep design process was performed to be cost effective and to converge to a final configuration that would give desired results.

Gas flowing through the quartz tube is much like pipe flow. To increase the velocity one would reduce the diameter, creating a converging nozzle. There is a limit, however, to how much one can constrict the flow before mass flow rate, $\dot{m}$ becomes constant. Even if the pressure downstream of the constriction is reduced even further, the mass flow through the nozzle cannot be increased unless the upstream pressure is increased. This condition is said to be *choked*. As seen in figure 3.1 there is a specific ratio of upstream pressure to downstream pressure, P/P_o of 0.528 (for $\gamma = 1.4$) [3] that inhibits choking. For inviscid flow there are no losses, but there when viscous effects are taken into account, P/P_o must be smaller than 0.528 to choke the flow.

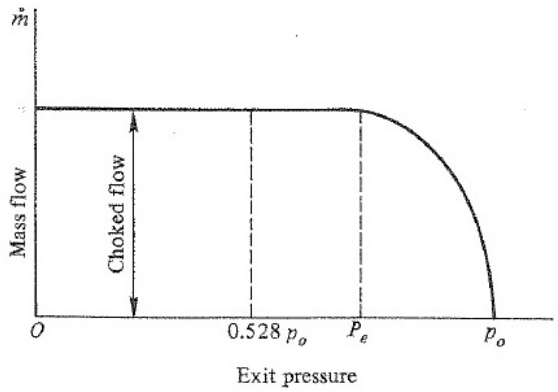

Figure 4.1: The mass flow rate reaches a constant value at $0.528P_o$ where the flow becomes choked, plotted for $\gamma = 1.4$ [4].

The equation below describes how area A is related to Mach number M,using the ratio of specifics heats, γ which not always a constant for reacting flows, and any variable marked with an asterisk denotes the condition at $M = 1$.

$$\frac{A}{A^*} = \frac{1}{M^2}\left(\frac{2}{\gamma+1}(1+\frac{\gamma-1}{2}M^2)\right)^{\frac{\gamma+1}{\gamma-1}}$$

When given a specific area ratio $\frac{A}{A^*}$, there will be two solutions for the Mach number. One will be subsonic and the other supersonic. This typically refers to the nozzle type being either converging or diverging. Figure 4.2 shows this relationship. We see that the desired Mach number is only a function of the area ratio for a given value of $\gamma = 1.4$ (diatomic).

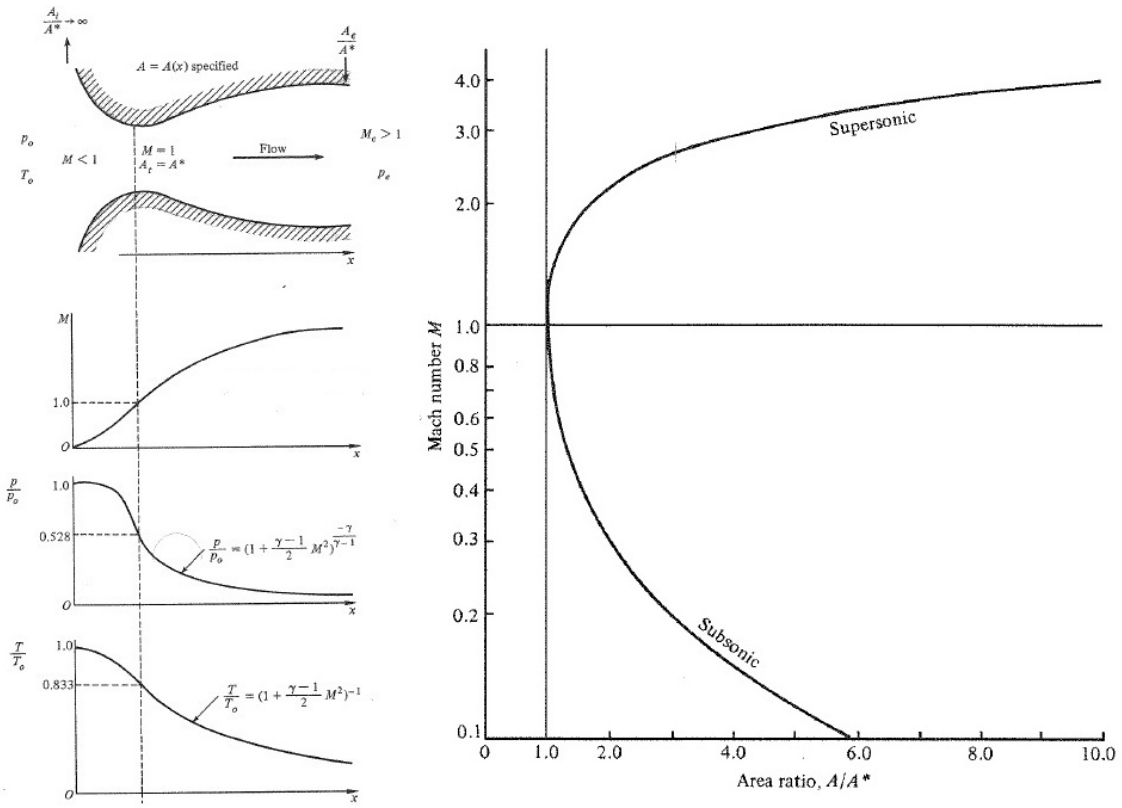

Figure 4.2: Relationship between pressure ratio, temperature ratio, area ratio, and Mach number [3].

Once the converging nozzle is choked, the only way to further increase velocity is to expand the area. This concept gives rise to a converging-diverging nozzle seen in the top left of figure 4.2, also known as a *de Laval nozzle*. In most cases, the highest Mach number is desirable, but the pressure ratio and temperature are often the limiting factors. The equations below describe this relationship. In the ICP torch, pressure is a function of torch input power and mass flow rate. Since there needs to be a minimum sustaining power to keep the torch running, regulating mass flow rate is the easiest way to adjust pressure. Corrections need to be made for γ because the value can range from 1.1 to 1.7 depending on the test gas and conditions being used.

$$\frac{P}{P_0} = (1 + \frac{\gamma - 1}{2} M^2)^{\frac{-\gamma}{\gamma - 1}}$$

$$\frac{T}{T_0} = (1 + \frac{\gamma - 1}{2} M^2)^{-1}$$

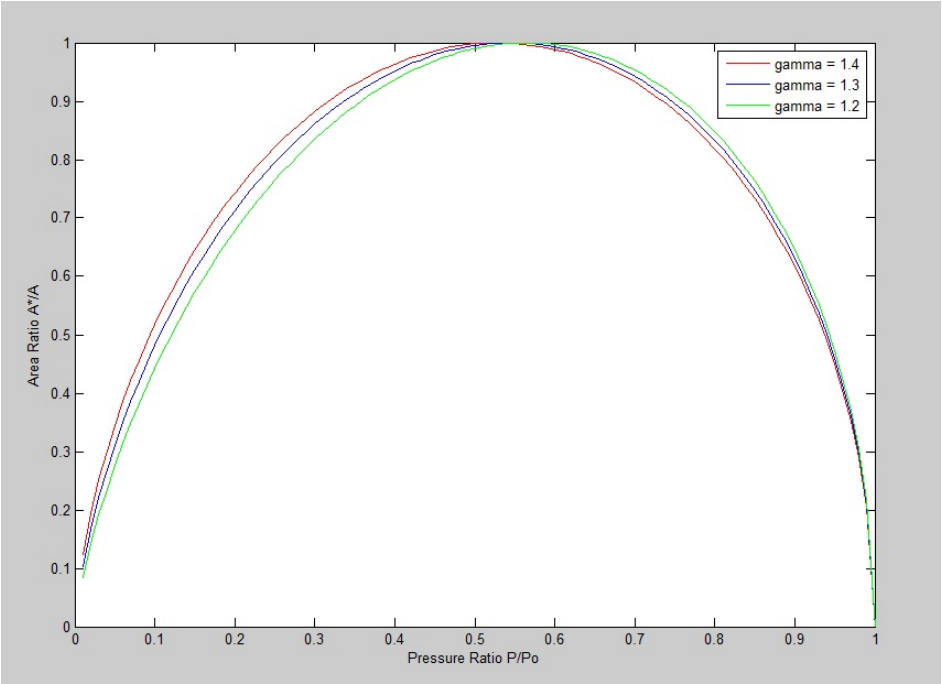

Figure 4.3: The relationship between area ratio and pressure ratio using different values of γ.

A common way to constrict pipe flow is by using an orifice plate. A small copper plate was squeezed together with a flange at the top of the quartz tube with an o-ring to prevent leakage. First, a 6 mm hole was drilled in the top of the orifice plate. Following the standard starting procedure described in chapter 2, argon was first attempted. The power supply could not couple to the gas and formed a glow discharge, which occurred during the orifice test. An iterative approach was taken by widening the hole on the orifice plate by 1.25 mm at a time decreasing the pressure upstream, and again restarting the torch. Unfortunately, the torch was

never able to run stably up to an orifice diameter of 18 mm. The upstream pressure is a function of how much electrical power is put into the flowing gas. When an abrupt change in pressure occurs, the torch cannot couple to the gas properly, and this creates the glow discharge. Also, due to a low Reynolds number, the boundary layer just upstream of the orifice plate pinches the flow constricting the hole diameter even more. It became apparent that not only does the flow need to expand, but there cannot be any abrupt changes in the streamline of the flow, meaning the angles turning the flow inward needed to be gentle.

Torch Model	Pressure drop in the torch (psig)		Max. total Pressure (psig)	Minimum allowable water flow Rate (l/min)	Sheath Argon gas flow (slpm)	Central Argon gas flow (slpm)	Plate Power (kW)
	Standard	Supersonic					
PL-35	50	80	100	26	60-80	20-30	30
PS-50	40	60	100	38	80-100	30-40	60
PS-70	40	NA	100	45	115-135	35-50	100
PS-100		NA			235-255	60-80	200

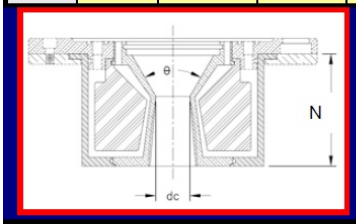

Model	dc (mm)	N (mm)	Θ
PL-35	12.33	43.82	60°
PS-50	20.74	68.67	60°
PS-70	26.08	76.03	60°

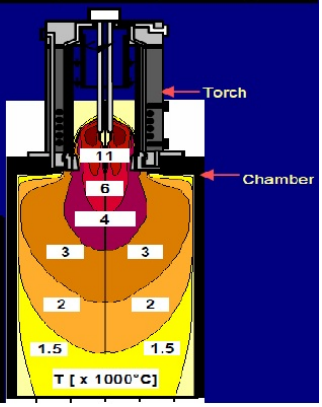

Figure 4.4: Tekna plasma supersonic system properties [15].

Tekna Plasma Systems Inc. uses a converging diverging nozzle to create a supersonic plasma for specific coating applications. Their PL-35 model is the smallest of such nozzles, and it uses a similar power supply with a similar setup when compared to the UVM ICP facility. The main differences with their design are the pressure and flow rate. The PL-35 expels plasma to atmospheric pressure whereas the UVM ICP torch exhausts to lower pressures from ranging from 2.67 to

26.7 kPa. Also the typical mass flow rate at UVM is 30-40 slm whereas the PL-35 operates at 60-80 slm. This design provided guidance for general shape and contour, taking into account its scale. Knowing that an orifice plate with a hole area twice the size of Tekna's nozzle throat could not operate effectively, it was apparent that the upstream gas needed to have space to expand.

4.2 First Iteration Nozzle

With the existing subsonic configuration, a downstream pressure of 21 kPa is typical while the torch is running. This suggests that the upstream subsonic operating pressure should be anywhere from 23 to 21 kPa. Knowing that this is the torch's "comfort zone", the nozzle needed to be designed to meet that criteria. As mentioned in Chapter 2, the torch is able to run outside of its normal range, but if the upstream pressure is below 13 kPa, then the quartz tube can melt, whereas if the pressure is above 29 kPa, the torch can extinguish. Placing a pitot tube with a manometer upstream of the quartz tube would be a good way to obtain the total upstream pressure. However, it is not ideal to place the pitot tube in the injection zone and owing to plumbing it is not clear where a tap would give P_0 reliably. A static downstream pressure tap is already in place. Even though this tap does not measure total pressure, it is quite close since dynamic pressure is low, especially when making measurements with the power supply turned off.

Four nozzles with embedded flanges were designed to be mounted onto the top of the tube adapter with an o-ring in the middle. The nozzles only varied in throat diameter and if they are designed to be supersonic or sonic. They all had a constant area ratio of $A_e/A^* = 2$. These were not meant to run with the power supply on as

it would melt them almost instantaneously due to material properties, rather they were used to resolve the upstream and downstream pressure parameters along with nozzle geometry. A general nozzle is shown in figure 4.5.

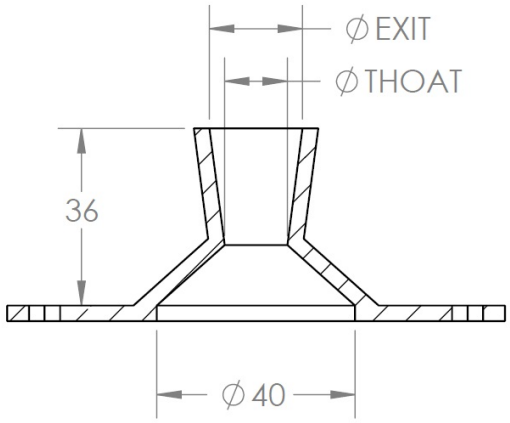

Figure 4.5: Model of first iteration nozzle.

A rapid prototyping machine was used to create the four nozzles with flanges to bolt up to the tube adapter. This machine creates a porous brittle ABS plastic model of the 3-D sketch. Since high pressure differentials were to be tested, a marine epoxy resign was used to seal the flange and nozzle. The throat diameters tested were ⌀ 12.7, 9.5, 6.4, and 5.1 mm.

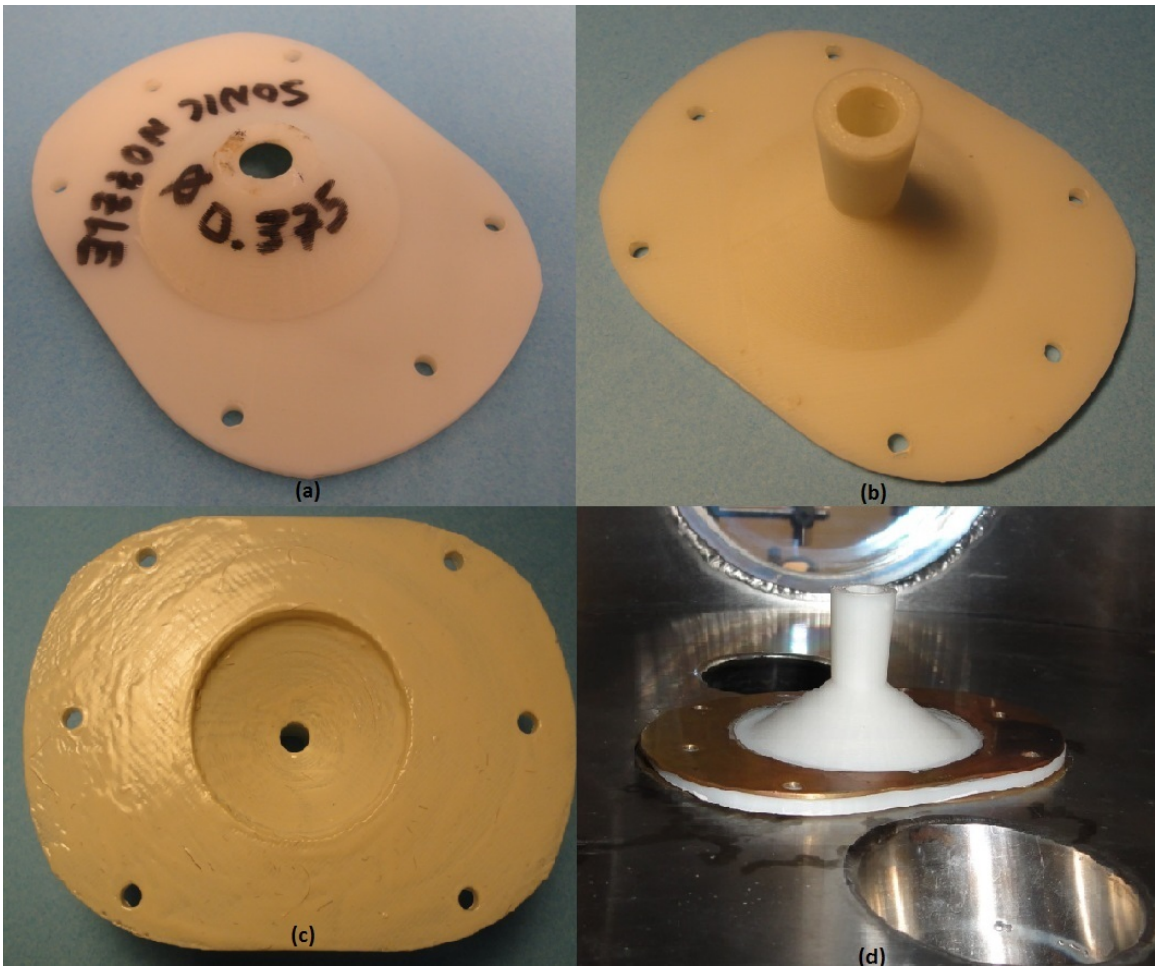

Figure 4.6: First iteration nozzles, (a) ⌀ 9.5 mm sonic nozzle,(b) ⌀ 9.5 mm supersonic nozzle, (c) ⌀ 6.3 mm bottom side of supersonic nozzle, (d) supersonic nozzle mounted in chamber with brass plate for even pressure distribution.

Figure 4.6 shows an example of the nozzles used. The ⌀12.7 mm nozzle was approximately scaled using a design taken from [11] (figure 3.73), shown in figure 4.7, the smaller diameter nozzles were scaled down maintaining the area ratio of 2. Since the height of the nozzle was kept constant, the upstream and downstream streamline angles needed to change. This made the ⌀12.7 mm nozzle more or less abrupt and the smaller diameter nozzles have a softer transition. Given that the plasma facility described in reference [23] was supersonic with their configuration; hypothetically, the ⌀12.7 mm nozzle could create a supersonic flow.

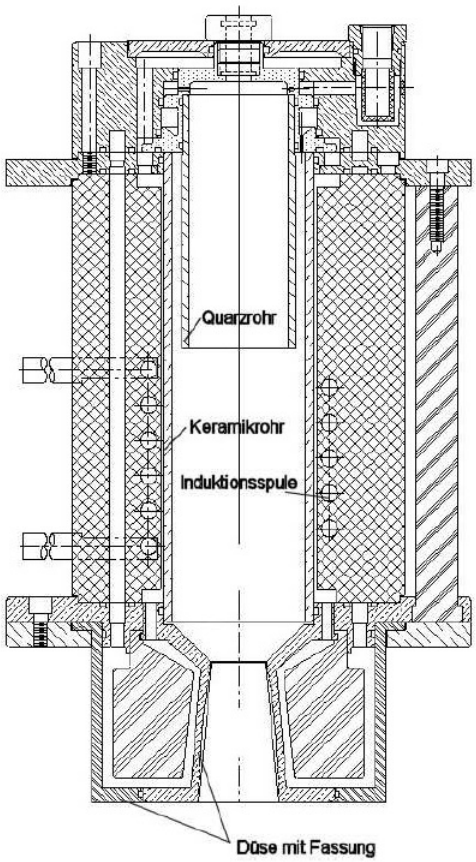

Figure 4.7: [22], figure 3.73 showing injection system and supersonic nozzle at the University of Stuttgart, Germany.

Several experiments were conducted to find the pressure ratio that would choke the nozzle. Having the test nozzle in place with a constant flow rate of 40 slm air, the downstream pressure was taken down in increments of 1.33 kPa starting at 20.0 kPa, while the upstream pressure was also monitored. When the upstream pressure stopped falling, and became constant, the nozzle was choked. Testing began with the sonic and supersonic nozzles starting from the largest diameter, ⌀12.7 to the smallest diameter of ⌀5.1 mm, although the sonic and supersonic nozzles did not show a difference in data.

The first two nozzles tested (⌀12.7 and 9.5 mm) did not show signs of choking,

however the ⌀6.4 and 5.1 mm did. The pressure data are shown in figure 4.8. The critical pressure ratio was nearly 2.8 for the ⌀6.4 mm nozzle, and about 1.6 using the ⌀5.1 mm nozzle. The downstream pressure transducer is relatively reliable with an accuracy of ± 0.3% of the reading, however the upstream transducer is not that accurate. A hand held model was used with an accuracy of ± 2.66 kPa, so when the choking occurs in the graph below, one must take into consideration the accuracy of the manometer and the upstream headloss. It should be noted that when choking occurred, there was a whistling noise coming from the chamber which was a good indicator of high speed flow.

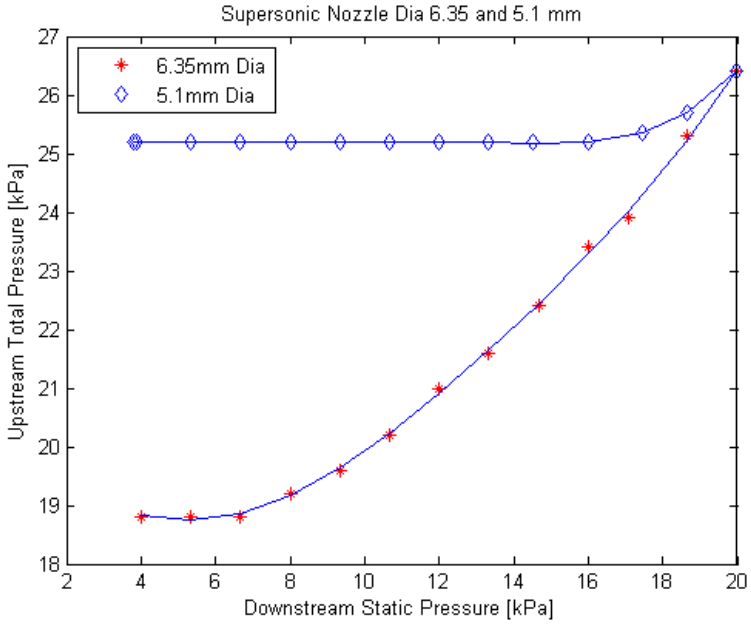

Figure 4.8: ⌀6.35 and 5.1 mm nozzle choking test, power supply not running.

4.3 Second Iteration Nozzle

Knowing that it is possible to choke a nozzle with a diameter of 6.4 mm with the power supply off, it should be possible to do the same when the power is on due to

the pressure rise. Nearing the end of a subsonic test, the power supply is turned off, but the gases are still flowing at the same rate making the pressure drop from 21.3 to 17.3 kPa inside the chamber. The volumetric ratio of the chamber to quartz tube is on the order of 100. This means that when the power supply is switched on, there is a large jump in pressure within the quartz tube, which can be used upstream of the nozzle's throat. As mentioned earlier, when the pressure goes over 29.3 kPa, the torch cannot run, consequently a larger nozzle can be put into place and could theoretically still choke the nozzle.

The second iteration nozzle was designed to be run when the power supply was turned on. The purpose of the design was to find a choking diameter, so a divergent section was not needed. The nozzle material needed to be able to withstand the high plasma temperatures. Owing to cost and availability, copper fittings were used because they fit well to a previous brass flange design described in chapter 2 used in the water cooled injection system. This made it possible to securely seat the nozzle on the tube adapter which is water cooled, providing a conduction path for a small amount of cooling. The nozzle was designed to find the choking diameter with the power supply running on 30 slm argon, and an air-argon mixture of 10 air 30 slm argon. Figure 4.9 shows the flange housing and the nozzle. A more detailed drawing of the nozzle can be seen in the Appendix.

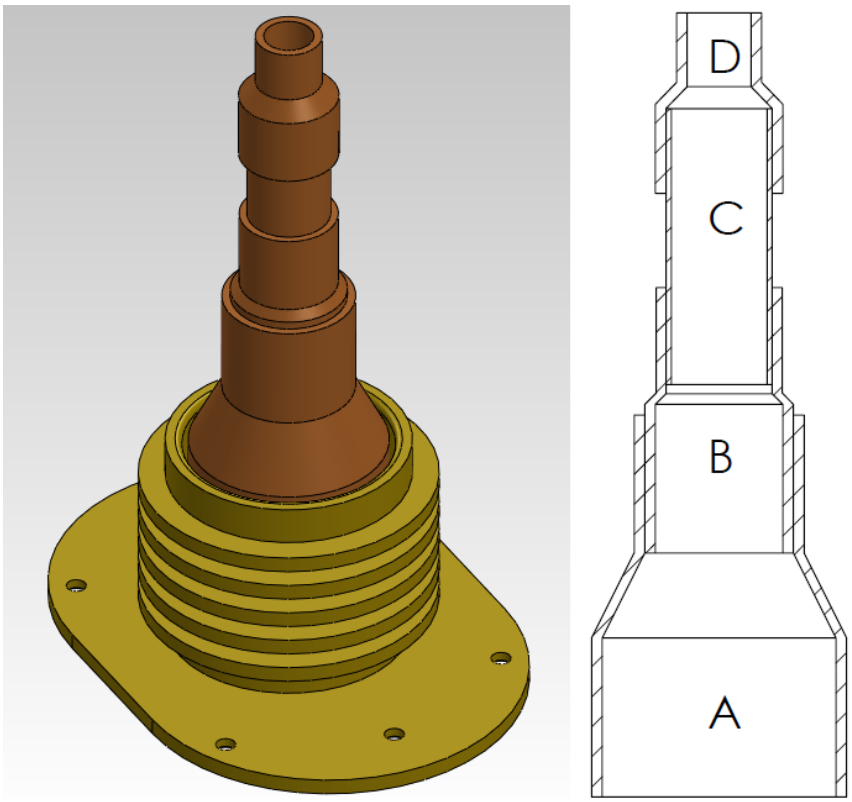

Figure 4.9: Second iteration nozzle assembly. On the left is the flange housing with the complete nozzle, the right shows how the nozzle is broken down into components.

This nozzle setup was convenient because of its interchangeable diameters. Beginning with sections A and B, the nozzle began testing with the same start up protocol as usual. With this configuration, the inside diameter was 16 mm. Argon, dilute argon-air, and pure air were able to run, however the diameter was too large and wasn't able to choke the flow. Section C was added making the diameter 14 mm. Again, the same protocol was used but only a flow rate of 30 slm argon was able to operate. The dilute mixture was attempted, but the torch extinguished prematurely. The mass flow rate was lowered, and a lower dilute mixture was achieved, but the torch still extinguished. It became apparent that owing to a low Reynold's number, the abrupt edges had an influence of the flow pattern. After the edges were smoothed over, another attempt was made with sections A, B and C. The

modification proved to be a success because an argon-air mixture was able to run at 30 slm argon and 30 slm air. However, when the power was increased and the mass flow was switched to 40 slm air, the torch extinguished. Three attempts were made to providing a sustained condition of 40 slm air, but with no success. Section D was omitted because constricting the flow even more would likely melt a quartz tube.

The nozzle may or may not have choked the flow, but the visual shock diamond pattern was not seen, meaning that either there was a normal shock wave standing in the nozzle, or it was simply not choking the flow. There was no method of cooling the nozzle aside from conduction through the bottom plate, making run times short. Total pressure was tested using the pitot tube and the results are shown in the table below. Total and static pressure were manipulated into a Mach

Table 4.1: Second iteration nozzle results.

2nd Iteration Nozzle Results Diameter = 14 mm			
Flow Rate [slm]	Static Pressure [kPa]	Total Pressure [kPa]	$\approx$ M
30 Ar	7.61	8.9	0.4
30 Ar 10 Air	6.7	10.0	0.8
30 Ar 30 Air	8.0	12.1	0.9

number via the total-static compressible equation shown earlier in this chapter. The nozzle Mach number results were adjusted because the pitot tube only senses total pressure, it does not have a static pressure tap on the side like most do. The raw static pressure is taken from the pressure tap inside the chamber which is a good approximation for low subsonic flow, but not approaching a Mach number of 1. A correction of 25% static pressure was added to the measured static pressure tap

data assuming exit flow was underexpanded. The actual Mach number could very well be higher or lower than the approximated Mach number. Also, as mentioned in chapter 3, the pitot tube will show a slightly higher total pressure due to a low Reynold's number. During testing, a whistling noise was heard from inside the chamber, just as the first iteration nozzle made, which could mean that it was close to choking. Another method of choking a nozzle is extending the pipe to a longer length making the boundary layer large enough until the nozzle chokes. Unfortunately, it would be difficult to find the exact choking location of the nozzle, and extending section C any further would result in geometry constraints of measuring the total pressure with a pitot tube.

If Tekna's supersonic design was scaled down to fit in the UVM facility, the throat diameter would be 12.7 mm. Knowing that the second iteration nozzle had a diameter of 14 mm, choking the flow required a smaller diameter nozzle, but not too small so that the torch could operate in its comfort zone. The next design would need to be more robust because this one glowed red after nearly 90 seconds of operation. A water cooled design was first considered, but not carried through due to complexity and machinability.

4.4 Third Iteration Nozzle

Learning from the previous nozzle designs, the ability to change geometry was important. The third iteration nozzle attempts to do so by having a standard nozzle holder, and having interchangeable nozzles to choke the flow. The holder would be placed into a salvaged flange from an earlier injector block design. Two 3.2 mm (1/8 inch) o-rings sealed the holder and flange concentrically. The nozzle inserts were

then able to move freely held by a set screw. Two inserts were chosen to have a throat diameter of ⌀11.4 mm (a 30% decrease in area from the previous iteration). The supersonic insert used an area ratio of 1.5. The actual dimensions can be seen in the appendix, but figure 4.10 shows the overall design.

This system was designed to have smooth contours and an adjustable nozzle height to allow for proper gas expansion. It is only cooled by conduction to the bottom flange, which is small, but the entire assembly has a large thermal mass to begin with. Knowing that the 2nd iteration nozzle was able to run for a relatively short period of time without melting, this system was expected to survive. The holder was machined from brass, and the nozzles from copper, both providing good thermal conductivity. An actual picture of the assembly can be seen in figure 4.11.

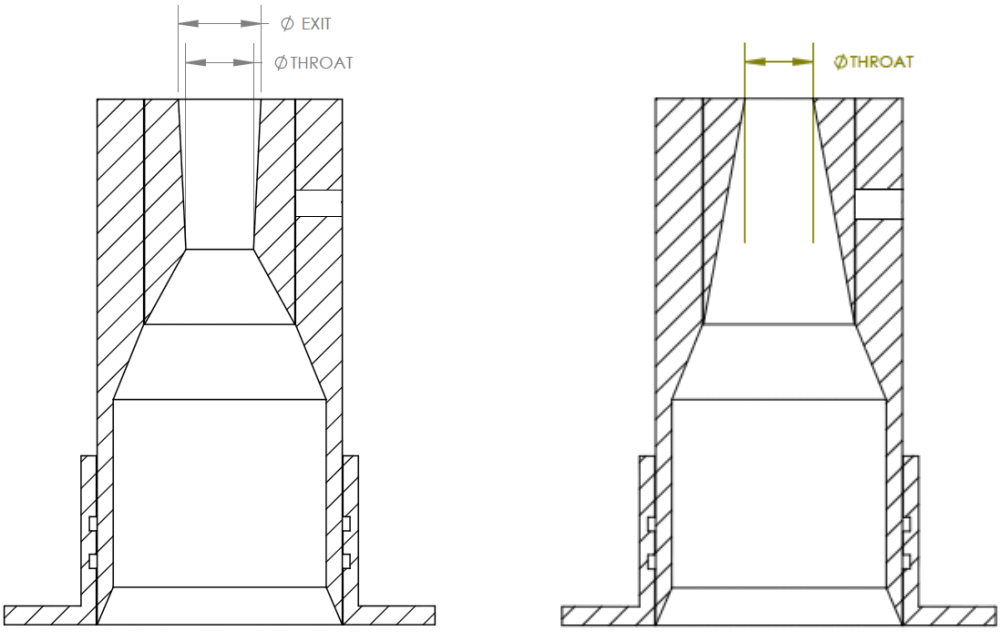

(a) Supersonic Configuration (b) Sonic Configuration

Figure 4.10: The supersonic and sonic nozzle configuration uses a set screw to remove nozzles and adjust height.

Figure 4.11: 3rd iteration nozzle assembly with supersonic insert.

The third iteration nozzle start up procedure deviated slightly because the chamber was kept at the lowest pressure (nearly 2.66 kPa for 30 slm argon) that the vacuum pump could maintain, making it possible to yield the highest Mach number with the given mass flow rate. The sonic nozzle flush with the nozzle holder was first attempted with pure argon as shown in figure 4.10(b). The argon plasma flow began to choke shortly after the flow rate was brought to 30 slm. To make sure the quartz wasn't suffering from a plasma discharge, the torch was quickly turned off and the injection system examined. No damage appeared in the injection region. The third iteration nozzle proved to be a success due to visible shock diamonds that appeared after the nozzle's exit, proving that the flow was indeed supersonic. Although the sonic nozzle only chokes the flow, since the chamber pressure was less than the plasma flow exit static pressure, the flow continued to expand creating a slightly higher Mach number. After argon was tested and showed sustainability, a dilute air mixture was introduced at 30 Ar 10 air slm. The power was also adjusted properly

to provide good coupling to the plasma. However, when the mixture was brought up from a 30-10 Ar-air to a 30-30 slm Ar-air, the torch extinguished. The system was consistent in not allowing for a 30-30 mixture as the upstream pressure neared 33 kPa. Efforts were made to keep the combined flow rates at 30 slm to achieve a pure air plasma, but with no success as the minimum sustaining power for air is much higher than argon, creating a larger upstream pressure. The supersonic nozzle was then put into place with the same start up procedure. The results only varied visually. The area ratio of 1.5 aimed at a pressure ratio of $P_0/P = 6.2$. This means that when running pure argon at 30 slm, the downstream chamber pressure was 2.72 kPa, and the upstream isentropic pressure was designed to be 16.9 kPa. Figure 4.12 shows sonic and supersonic operation during a pure argon test. Note how the sonic nozzle produces a larger exit angle than the supersonic nozzle due to underexpansion. Shock diamonds are clear in the rendered images. They act to equalize the flow pressure to the ambient pressure by means of expansion and compression waves. Before the first shock diamond, the nozzle produces an underexpanded flow, which will need to expand further to the chamber pressure. This is done by a Prandtl-Meyer expansion fan, but when the pressure becomes too low downstream of the expansion fan, it is turned in again using a compression wave. This pattern is repeated downstream creating shock diamonds due to Mach waves intersecting. This phenomena can be seen on a military aircraft jet engine during takeoff.

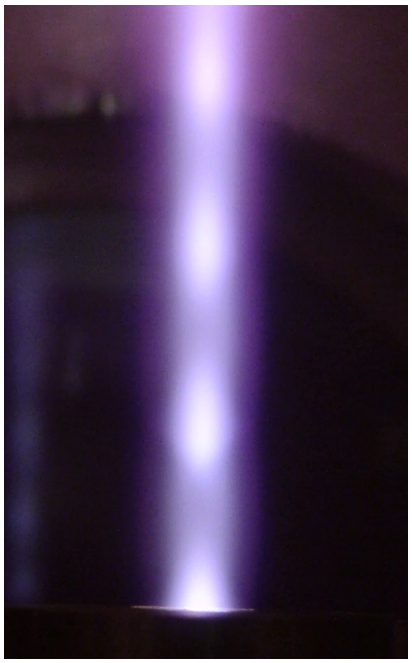

(a) Sonic argon raw image

(b) Supersonic argon raw image

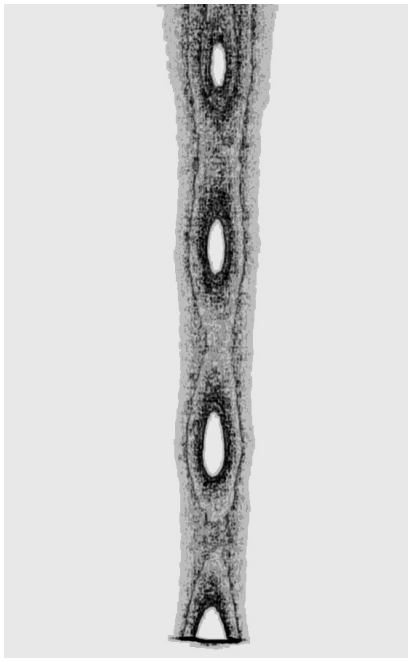

(c) Sonic argon rendered image

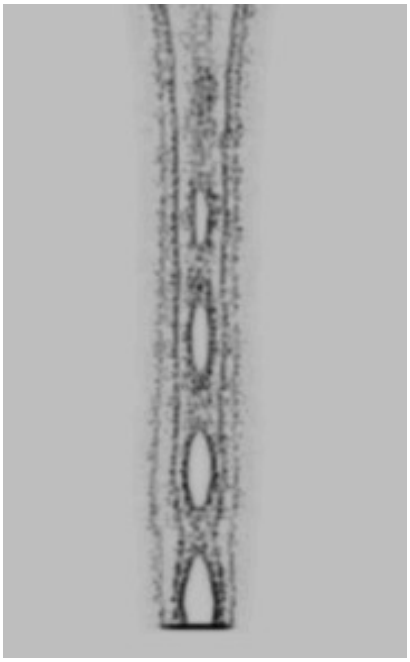

(d) Supersonic argon rendered image

Figure 4.12: Figures (a) and (b) show raw images of the sonic and supersonic nozzle. (c) and (d) are the rendered images to increase contrast and to visualize the shock diamonds.

4.5 Nozzle Results

Three different methods were used to evaluate the Mach number corresponding to each nozzle and test gas. The pitot tube was first used to measure the total pressure for each condition. The chamber pressure is also measured using the static pressure tap. Even though the static pressure of the flow is different from the ambient pressure, owing to underexpansion, we can assume that a slightly lower Mach number is in order from the calculated one, especially with the sonic nozzle. Had a pressure tap been inserted upstream of the nozzle's throat, a far more accurate upstream total pressure reading could have been taken. Instead the upstream total pressure was taken through a pitot tube in the injection system. Suffering from head losses, the upstream measured reading was likely higher than the actual pressure in the quartz tube. The second method uses the exit angle of the flow to calculate the local Mach number after expansion. This method calculates the expansion part, not compression. The third analysis is done by measuring the length of the first shock diamond, and width of the fully expanded gas. By use of a simple formula, one can deduce the average Mach number. This is the least accurate method however, because in our case shock diamonds are not clearly defined.

Using the pitot tube to calculate a Mach number is fairly straight forward. The pitot tube was mounted onto the gooseneck probe at its highest position. when operation was stable, the probe was swung into place for a few seconds, and then quickly removed to avoid overheating. The pressure tap that is normally inside the chamber was attached to the pitot tube. When the gooseneck probe was out of the flow, the pressure tap measured static pressure, and when in the flow it measured total pressure. The control system for the facility logs pressure in a file along with

all other incoming data. Knowing the static and total pressure, recall the Rayleigh-Pitot tube formula from chapter 3 to find Mach number.

$$\frac{P_{02}}{P_1} = \frac{P_{02}}{P_2}\frac{P_2}{P_1} = \left(\frac{(\gamma+1)^2 M_1^2}{4\gamma M_1^2 - 2(\gamma-1)}\right)^{\frac{\gamma}{\gamma-1}} \left(\frac{1-\gamma+2\gamma M_1^2}{\gamma+1}\right)$$

In this case γ may vary with temperature, pressure and different combinations of gases. NASA's CEA program was used to calculate such parameters with the conditions matching the ambient test environment. For example, ρ and γ were calculated for the sonic nozzle running on pure argon using a temperature of 5000 K and a pressure of 2.7 kPa. CEA has a built in function that allows for dissociation at required conditions, making it more accurate for plasma applications. The following uses the compressible supersonic pressure equation to find the Mach number for the conditions below. The Bernoulli equation was used to evaluate the subsonic system because it is believed to be below $M < 0.3$, but the sonic and supersonic nozzles required the Rayleigh-Pitot relation. The results are shown below for the subsonic, sonic, and supersonic nozzle.

Table 4.2: Pitot tube calculated results for subsonic, sonic, and supersonic nozzle setups using the Rayleigh-Pitot relation.

	Flow Rates [slm]		
	30 Ar	30 Ar 10 Air	40 Air
$M_{Subsonic}$	0.15	0.17	0.17
M_{Sonic}	1.31	1.41	
$M_{Supersonic}$	1.43	1.54	

The next method uses the angle at which the flow is exiting the nozzle to determine Mach number. This can be seen in underexpanded or overexpanded nozzles where

the exit pressure does not match the ambient pressure, turning the flow. In our case of underexpansion seen in the sonic nozzle, the flow turns outward via an expansion fan. An infinite number of Mach waves are responsible for doing so, and is dictated by the difference of Mach number before and after the expansion fan. The equation relating the angle and Mach number is shown below, called the Prandtl-Meyer equation. The angle ν is an arbitrary angle chosen so $\nu(1) = 0$. It is only used to find the difference of two angles with associated Mach numbers, as seen in the next equation.

$$\nu(M) = \sqrt{\frac{\gamma+1}{\gamma-1}} arctan \sqrt{\frac{\gamma-1}{\gamma+1}(M^2-1)} - arctan\sqrt{M^2-1}$$

$$\theta = \nu(M_2) - \nu(M_1)$$

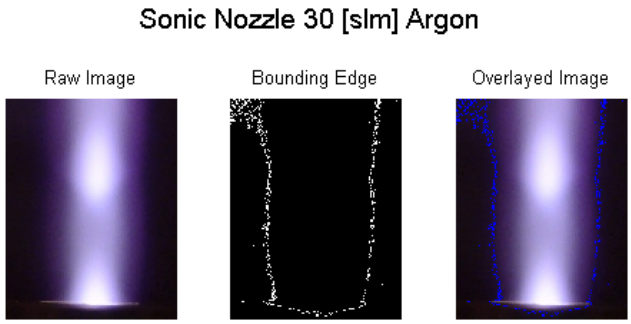

Figure 4.13: Detecting the edge of the flow using Matlab's image processing.

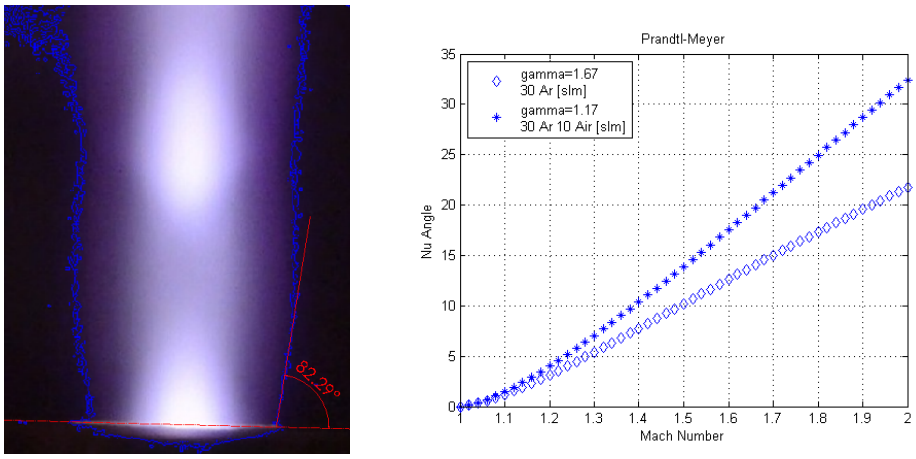

(a) (b)

Figure 4.14: Measurement of exit angle after a sonic pure argon test (a), evaluation of the corresponding Mach number using the graph of M vs. ν for different γ values (b).

Figure 4.14 shows the angle of the exit flow using the sonic nozzle during an argon test. Since we know that the Mach number right at the exit is M=1, then $\nu(M_1) = 0$ and the equation becomes $\theta = \nu(M2)$. The graph can be directly used to find the Mach number of the flow. The supersonic nozzle case is a little different because the exit Mach number is not M=1, but when the same analysis is done using an image analysis tool to find the edge, it's difficult to find an angle that deviates much from 0. Although the supersonic nozzle may not be the perfect expansion case, it can be approximated as such. In this case the ambient pressure is very close to the exit pressure and the area ratio equation can be used assuming perfect expansion. This is a high estimate due to having such a low Reynold's number, which produces much dissipation.

The next method involves taking a closer look at the shock diamonds. Using the wavelength from one shock diamond to another, and knowing the fully expanded diameter, the Mach number can be found using the Prandtl-Pack relation [29], [31].

Only the first shock wave should be evaluated because dissipation and blurring downstream will increase error. With figure 4.15 showing how to measure the shock diamond, and using the Prandtl-Pack relation below, one can find the Mach number.

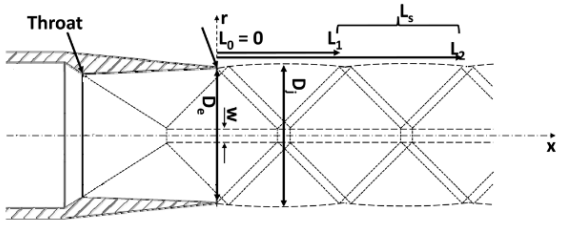

Figure 4.15: A diagram of the length and diameter of shock waves downstream of the nozzle [29].

$$M(L_s, D_j) = \left(\sqrt{\frac{L_s \mu}{D_j \pi}} + 1 \right)^2$$

Where $\mu = 2.405$. The relation is convenient because of it's simplicity, and can be quite accurate given the certainty of the shock waves. This relation is highly useful in CFD, and Schlieren images where generated figures have good contrast and are as accurate as the user allows them to be. However, the plasma contrast expelling from a nozzle is difficult to resolve when searching for definite Mach waves. Nevertheless, it is possible to make a guess with the help of image processing techniques. After measuring the center distance between the first two shock diamonds, the sonic and supersonic nozzle Mach numbers compared closely with the pitot tube method.

After using three different methods to find the Mach number, a good estimate can be approximated for each case, though uncertainty is relatively high for some methods. The graph below shows the results for the three different methods and an estimate of the uncertainty for each. It seems that even though there was no static pressure tap on the pitot tube, this was the most accurate way to estimate a Mach

number. Arguably the least accurate was the exit angle on the supersonic nozzle, because there was no known outlet Mach number, and the area ratio estimate is assuming an isentropic process. The cumulative results are shown below in figure 4.16. Note that the Prandtl-Meyer uncertainty is only downward because we are assuming a perfect isentropic system.

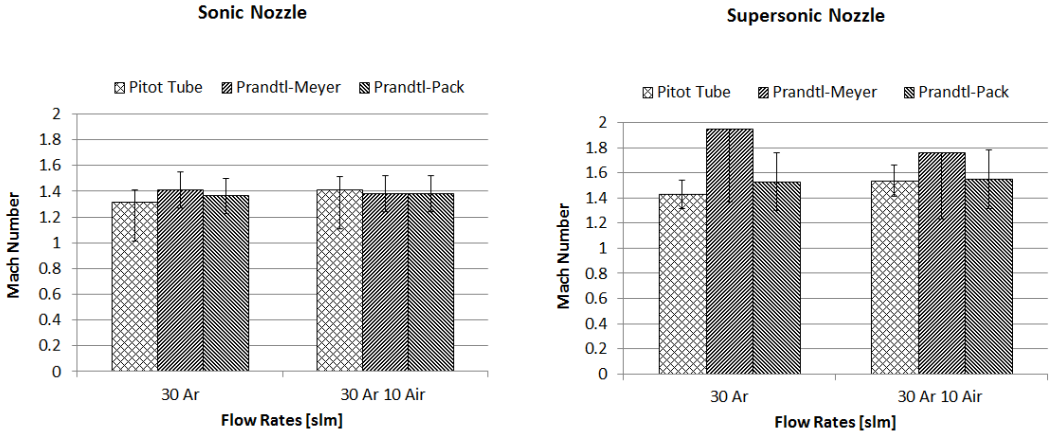

(a) (b)

Figure 4.16: The pitot tube, Prandtl-Meyer, and Prandtl-Pack methods are shown for the sonic (a) and supersonic nozzles (b) to find the corresponding Mach numbers.

Heat flux was also tested during sonic and supersonic operation with the slug calorimeter. As mentioned earlier, a pure air plasma condition could not be created, meaning that no comparison could be made between the subsonic and supersonic pure air case. 30 slm argon and 30-10 slm argon-air mixture were tested using the subsonic, sonic, and supersonic system. Recall the heat equation from chapter 1 [21], [20].

$$\frac{\ddot{q_w} = 0.76(Pr)^{-0.6}(\rho_s\mu_s)^{0.4}(\rho_w\mu_w)^{0.1}(\beta)^{0.5}(h_e - h_w) \quad \textit{Supersonic}}{\ddot{q_w} = 0.76(Pr)^{-0.6}(\rho_s\mu_s)^{0.5}(\beta)^{0.5}(h_e - h_w) \quad \textit{Subsonic, incompressible}}$$

Where now μ for the supersonic case will go down slightly because of temperature

dependence, which also effects the Prandtl number slightly. Enthalpy will very close to the same between supersonic and subsonic operation due to the velocity being compensated for by the translational temperature. As mentioned earlier, we are left with the velocity gradient du/dx for comparison, but this needs a correction term for different geometries and Mach numbers, where the corner radius of the probe has a considerable impact. Using the equation below with the graph from figure 7-6 in [43], one can deduce an approximated correction.

$$\frac{KD}{V_\infty} = f(M_\infty, bodyshape) \qquad\qquad K = \beta = du/dx$$

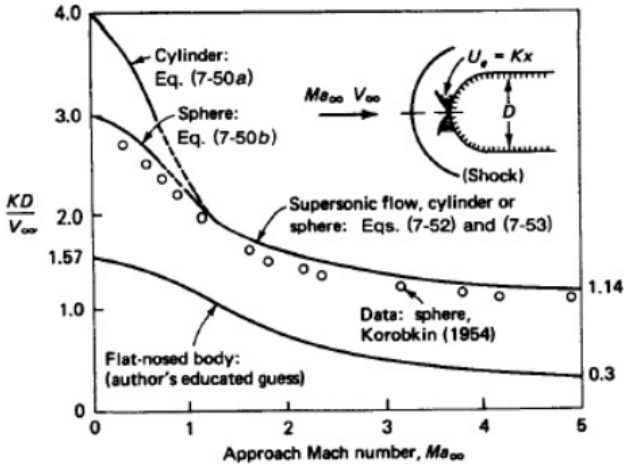

Figure 4.17: Affects of nose radius and Mach number on velocity gradient. Figure 7-6 in [43].

Due to the UVM ICP torch standardized sample design, a approximation for $\left(\frac{KD}{V_\infty}\right)_{SS} \approx 2.5$ and for $\left(\frac{KD}{V_\infty}\right)_{Sub} \approx 1.6$ is used. Now we have,

$$\frac{\ddot{q}_{SS}}{\ddot{q}_{Sub}} \approx \sqrt{\frac{(du/dx)_{SS}}{(du/dx)_{Sub}}} \approx \sqrt{\frac{2.5V_{\infty,SS}}{1.6V_{\infty,Sub}}}$$

For example, knowing the Mach number to around 1.4 and 0.15 for the sonic, and subsonic system, and the local sound speed (from NASA's CEA) shown in table 5.1,

the equation can be solved. The comparison between sonic and subsonic flow yields a calculated ratio 2.4 for the heat flux, which is very close to the measured value ratio when comparing to figure 4.18. Although the slug calorimeter has an estimated uncertainty of roughly 5-10%, the sonic and supersonic nozzles proved to be a success for raising the heat flux of the facility.

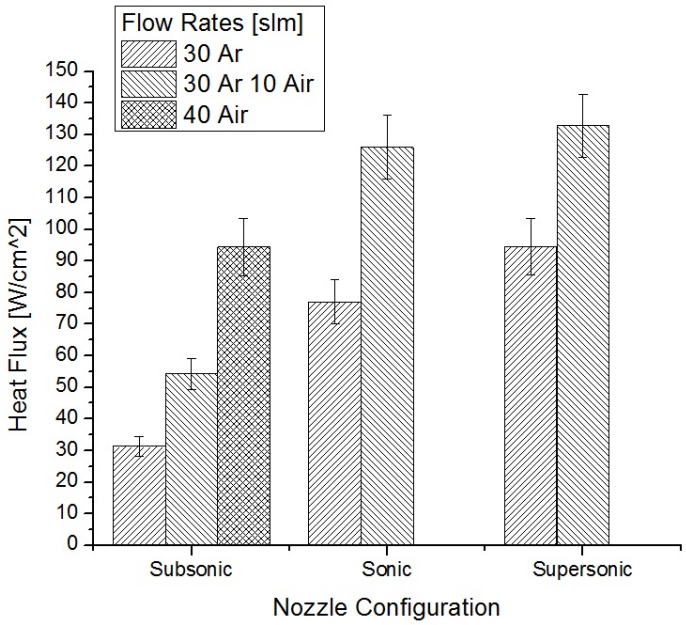

Figure 4.18: Subsonic, sonic, and supersonic heat flux compared by flow rates.

Chapter 5

Conclusion

Table 5.1: Overall UVM ICP torch subsonic and supersonic characteristics.

	Nozzle Configuration						
	Subsonic			**Sonic**		**Supersonic**	
$\dot{m}$ [slm]	30 Ar	30-10 Ar-Air	40 Air	30 Ar	30-10 Ar-Air	30 Ar	30-10 Ar-Air
$P_{Total}[kPa]$	24	24	24	23.3	26	25.3	28
P_{Static}	21.3	21.3	21.3	2.9	3.7	2.7	3.7
$P_{Dynamic}$	0.36	0.39	0.36	5.9	8.1	6.8	8.3
ρ $[Kg/m^2]$	0.021	0.017	0.011	0.0026	0.0029	0.0026	0.0029
γ	1.67	1.17	1.23	1.67	1.17	1.67	1.17
a [m/s]	1320	1240	1470	1320	1220	1320	1220
M_{pitot}	0.15	0.17	0.17	1.31	1.41	1.43	1.54
V[m/s]	195	205	245	1700	1850	1900	1900
$\ddot{q}$ $[W/cm^2]$	31	54	94	77	126	95	133

Although the water cooled injection system did not operate as anticipated, it gave much insight as to how the existing system can be modified. The overall goal was to be able to run the power supply at a higher power for a longer duration. Due to the relatively low scale of the power supply, the facility needs to be as efficient as possible. We learned that adding a water cooled system would hinder the power output, lowering efficiency. Failing o-rings were the largest contributer to limited test time, but the sealant and convective air cooling system raised test times and lowered maintenance.

Heat flux methods have now been examined showing the slug calorimeter to the most reliable. When testing heat flux, the three calorimeters in the UVM ICP facility are not at all conclusive, other designs could be adapted to the existing components. Owing to size constraints, the water cooled calorimeter should be redesigned to yield a higher accuracy, and suppress noise issues.

A new milestone was achieved by expanding the facility to operate supersonically, and thereby showing how heat flux scales with velocity gradient. A larger throat diameter would probably be necessary to allow for a full air plasma in the supersonic nozzle. A cooling system could also be installed if longer test times were of interest.

A large amount of work is still needed to understand the power supply and proper gas coupling. The facility could be improved if coupling efficiency were examined, and pressure could be brought past 26.67 kPa.

References

[1] Abeele, David V. "An Efficient Computational Model for Inductively Coupled Air Plasma Flows under Thermal and Chemical Non-Equilibrium." VKI Thesis (2000)

[2] Allen, Julian H., Eggers, Jr. A.J. "A Study of the Motion and Aerodynamic Heating of Ballistic Missiles Entering the Earth's Atmosphere at High Supersonic Speeds," *National Advisory Committee for Aeronautics* Report 1381, (1957)

[3] Anderson, John D. *Hypersonic and High-Temperature Gas Dynamics.* (American Institute of Aeronautics and Astronautics, Inc.,Reston, Virginia, 2006)

[4] Anderson, John D. *Modern Compressible Flow:With Historical Perspective.* (New York:MeGraw-Hill, 2003)

[5] ASTM Standard E422, 2005, "Standard Test Method for Measureing Heat Flux Using a Water-Cooled Calorimeter," *ASTM International* E422-05 pp. 684-688

[6] ASTM Standard E457, 2002, "Standard Test Method for Measuring Heat-Transfer Rate Using a Thermal Capacitance (Slug) Calorimeter" *ASTM International* E457-08 pp. 704-709 27

[7] ASTM Standard E459, 2002, "Standard Test Method for Measuring Heat Transfer Rate Using a Thin-Skin Calorimeter" *ASTM International* E459-05 pp. 718-724

[8] ASTM Standard E511, 2007, "Standard Test Method for Measuring Heat Flux Using a Copper-Constantan Circular Foil, Heat Flux Transducer" *ASTM International* E511-07 pp. 777-786

[9] ASTM Standard E639, 2002, "Standard Test Method for Measuring Total-Radiance Temperature of Heated Surfaces Using a Radiation Pyrometer" *ASTM Internationa*l E639-78 pp. 833-839

[10] Auweter-Kurtz, Monika, Wegmann, Thomas. "Overview of IRS Plasma Wind Tunnel Facilites" (paper presented at the RTO AVT Course on "Measurement Techniques for High Enthalpy and Plamsa Flows", Rhode-Saint-Genese, Belgium,1999)

[11] Bottin et al.,"The VKI Plasmatron Characteristics and Performance" Von Karman Inst for Fluid Dynamics (Rhode-Saint-Genese,Belgium,2000)

[12] Boulos, I. Maher "The inductively coupled R.F. (radio frequency)". 1985, *Pure and Appl. Chem.*, Vol. 57,No.9,pp. 1321-1352, 1985

[13] Drause, Lloyd N and Glawe, George E. "A Review of the Mass-Flux Probe" *NASA Technical Memorandum* TM X-52974 (1971)

[14] Dowding, Kevin J., Blackwell, Ben F. and Cochran, Robert J. "Study of Heat Flux Gages Using Sensitivity Analysis," Thermal Sciences Dept., Albuquerque, New Mexico SAN098-1758C (1998)

[15] Bouchard, Eric. email message to author, November 26, 2012

[16] Esposito et al. "Design of Slug Calorimeters for Re-Entry Tests" (Paper presented at University of Naples Federico II, Via Claudio, 21-80125 Naples, Italy, 2010)

[17] Gudmundsson, J.T. and Lieberman, M.A. "Magnetic induction and plasma impedance in a cylindrical inductive discharge," *Plasma Sources Sci. Technol.* Volume 6 pp. 540-550 (1997)

[18] Gulgan, A. "Heat Flux Measurements in High Enthalpy Flows" (paper presented at the RTO AVT Course on "Measurement Techniques for High Enthalpy and Plasma Flows", Rhode-Saint-Genese, Belgium, 1999)

[19] FAA:Aviation Industry, last modified February 19, 2013, www.faa.gov

[20] Fay, J.A. and Riddell, F.R. "Theory of Stagnation Point Heat Transfer in Dissociated Air," Journal of the Aeronautical Sciences Volume 25, No. 2, (1958)

[21] Fletcher, D.G. and Playez, M., "Characterization of Supersonic and Subsonic Plasma Flows". AIAA (Rhode-Saint-Genese,Belgium,2006), Von Karman Institute for Fluid Dynamics ed.

[22] Herdrich, Georg F., Auweter-Kurtz, M., Kurtz, H., "New Inductively Heated Plasma Source for Reentry Simulations". *Journal of Thermophysics and Heat Transfer*, Volume 14, No. 2 (2000) (244-249)

[23] Herdrich, Georg F. "Aufbau, Quali

kation und Charakterisierung einer induktivbeheizten Plasmawindkanalanlage zur Simulation atmosphrischer Eintrittsmanver" (Ph.D diss., University of Stuttgart, 2004)

[24] Lees, Lester. " Laminar Heat Transfer Over Blunt-Nosed Bodies at Hypersonic Flight Speeds," *The Ramo-Wooldrige Corporation*, Los Angeles, and California Institute of Technology, Pasadena, Calif. 259-274 (1956)

[25] Lieberman, M. A., *A Mini-Course on the Principles of Plasma Discharges* class notes (2003)

[26] Lieberman, M. A. and Lichtenberg, A. J., *Principles of Plasma Discharges and Material Processing*, (John Wiley and Sons, New York) 1994, Chap. 12.

[27] National High Magnetic Field Laboratory. (Last modified: January 21, 2009) www.magnet.fsu.edu

[28] Morsli, Mbark and Proulx, Pierre. "Two-temperature chemically non-equilibrium modelling of an air supersonic ICP," *Journal of Physics D: Applied Physics* Volume 40, pp. 4810-4828 (2007)

[29] Munday et al, "Flow Structure and Acoustics of Supersonic Jets from Conical Convergent-Divergent Nozzles". *Physics of Fluids*, Volume 23, 116102-1 (2011)

[30] Nawaz, Anuscheh and Herdrich, Georg. "Impact of plasma tube wall thickness on power coupling in ICP sources," *Plasma Sources Science and Technology* Volume 18 (2009)

[31] Pack, D.C. "A Note on Prandtl's Formula for the Wave-Length of a Superosnic Gas Jet," *Quarterly Journal of Mechanics and Applied Mathematics* Volume 3, Part 2 (1950)

[32] Roger, Launius D. and Jenkins, Dennis R., *Coming Home: Reentry and Recovery from Space*. (Washington, DC:National Aeronautics and Space Administration, 2012)

[33] Olivier Chazot, Jorge Miguel Periera Gomes and Mario Carbonaro. "Characterization of a "Mini-Plasmatron" Facility by Pitot Probe Measurements," *AIAA* 98-2478 (1998)

[34] Owens, W.P., Uhl, J., Dougherty, M. and Fletcher, D.G. "Devolopment of a 30 kW Inductively Coupled Plasma Torch Facility for Aerospace Material Testing," (Presented at the 10th AIAA/ASME Joint Thermophysics and Heat Transfer Conference, Chicago, Illinois, June 28 - July 1, 2010)

[35] Owens, W.P. "Development of a 30 kW Inductively-Coupled Plasma Torch for High Temperature Aerospace Material Testing at UVM" (Master's thesis, University of Vermont, 2010)

[36] Park, Chul. "Laboratory Simulation of Aerothermodynamic Phenomena: A Review," *AIAA 92-4025* (1992)

[37] Park, Chul. "Properties of Inductively Coupled Plasma Source with Helical Coil," *Transactions on Plasma Science* Volume 28, No. 2 (2000)

[38] Sember, Viktor, Gravelle, Denis V. and Boulos, Maher I. "Spectroscopic study of a supersonic plasma jet generated by an ICP torch with a convergent-divergent nozzle," *Journal of Physics D: Applied Physics* Volume 35, pp. 1350-1361 (2002)

[39] Stephenson, W.B. "Use of the Pitot Tube in Very Low Density Flows," *Arnold Engineering Development Center*, Tennessee AEDC-TR-81-11 (1981)

[40] Takeshi et al, "110 kW New High Enthalpy Wind Tunnel heated by Inductively-Coupled-Plasma," AIAA *2003-7023* White, Frank M. Fluid Mechanics. (New York:McGraw-Hill, 2008)

[41] Uhl, Juergen. "Pyrolysis Investigation of an ICP Torch Facility" (Master's thesis, University of Vermont, 2012)

[42] White, Frank M. *Fluid Mechanics* (New York: McGraw-Hill, 2008)

[43] White, Frank M. *Viscous Fluid Flow* (New York:McGraw-Hill, 1974)

[44] Zinn, S. and Semiatin S.L. *Elements of Induction Heating:Design, Control, and Applications*. (Palo Alto, CA: Electric Power Research Institute, 1987)

[45] Zoby, Ernest V. "Empirical Stagnation-Point Heat-Transfer Relation in Several Gas Mixtures at High Enthalpy Levels," *NASA Technical Note* Tn D-4799 (1968)

[46] Zoby, Ernest V. and Sulliban, Edward M. "Efects of Corner Radius on Stagnation-Point Velocity Gradients on Blunt Axisymmetric Bodies," *NASA Langly Research Center*, Hampton, Virginia Volume 3, No. 10, (1966)

Appendix

SECTION A-A

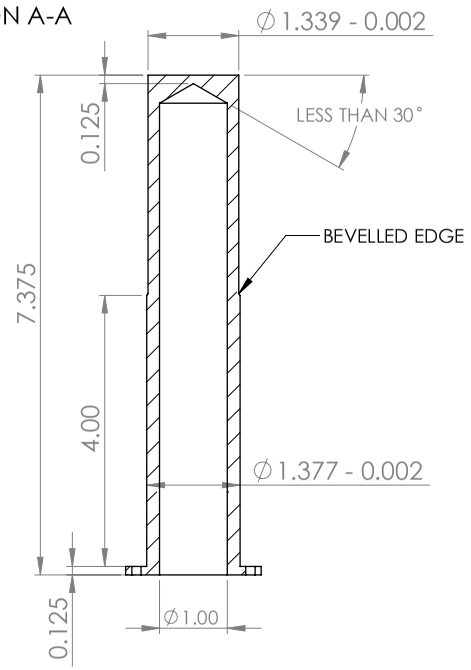

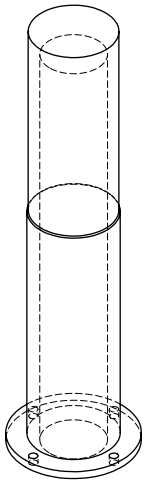

DRILL THRU
FOR 6-32 BOLT
1.682" DBC
TYP. (4) AT 90° APART

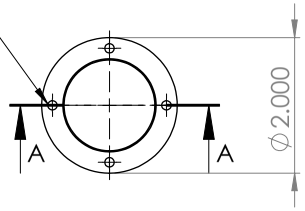

MATERIAL IS BRASS

TOLERANCE:

.x	±0.025
.xx	±0.01
.xxx	±0.005

INJECTOR INSERT	
NAME: SILAS SMITH	06/18/2012
PHONE: 802-274-2602	

The University of Vermont

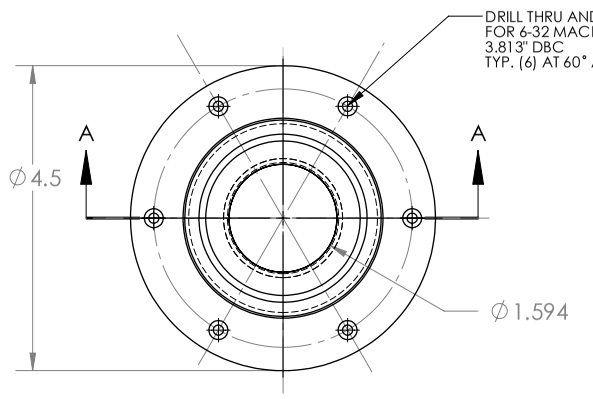

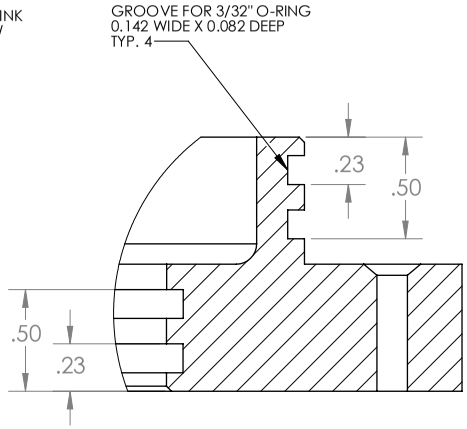

DETAIL B
SCALE 1.5 : 1

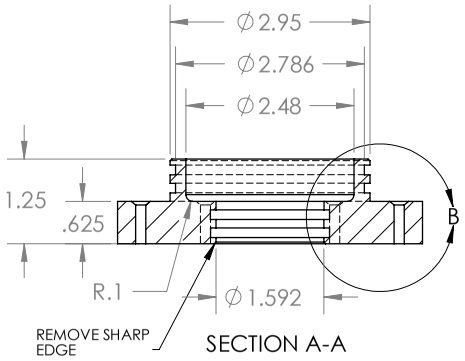

SECTION A-A

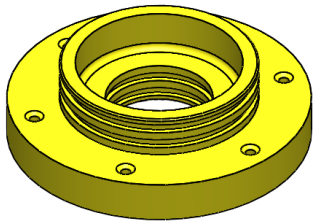

MATERIAL IS BRASS

TOLERANCE:
.x ±0.025
.xx ±0.01
.xxx ±0.005

BOTTOM	
NAME: SILAS SMITH	03/03/2011
PHONE: 802-274-2602	

The University *of* Vermont

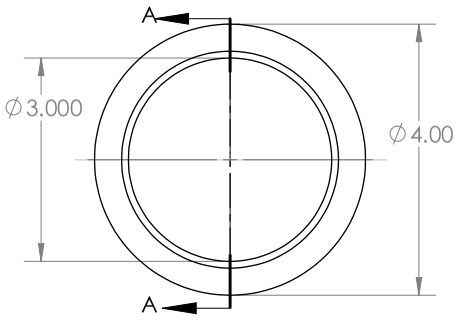

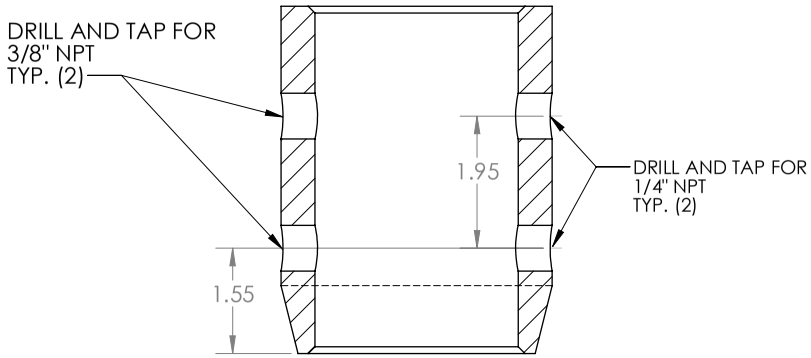

SECTION A-A

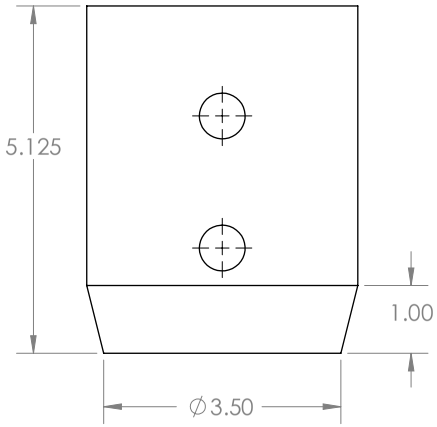

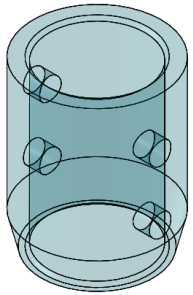

MATERIAL IS CLEAR POLYCARBONATE

TOLERANCE
.x ±0.025
.xx ±0.01
.xxx ±0.005

CYLINDER	
NAME: SILAS SMITH	05/31/2011
PHONE: 802-274-2602	

The University *of* Vermont

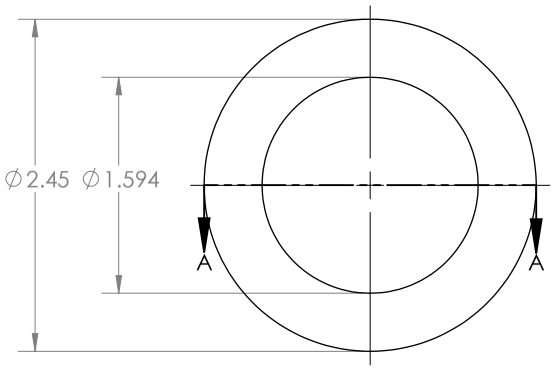

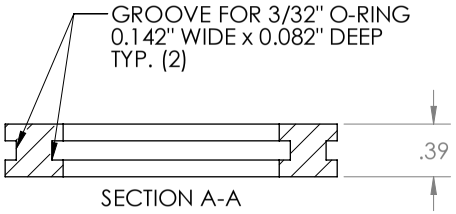

MATERIAL IS PTFE

TOLERANCE:
.x ±0.025
.xx ±0.01
.xxx ±0.005

INSULATOR	
NAME: SILAS SMITH	05/31/2012
PHONE: 802-274-2602	

The University *of* Vermont

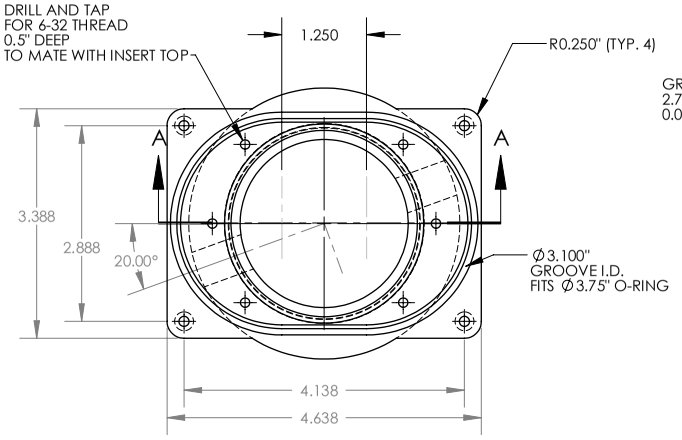

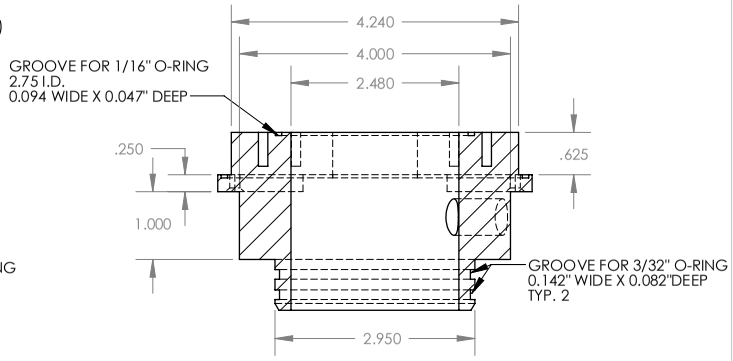

SECTION A-A

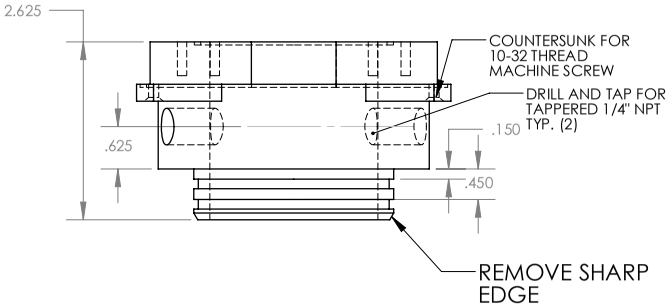

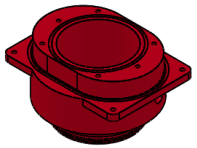

MATERIAL IS ULTEM

TOLERANCE
.x ±0.025
.xx ±0.01
.xxx ±0.005

BOTTOM INSERT	
NAME: SILAS SMITH	05/31/2012
PHONE: 802-274-2602	

The University *of* Vermont

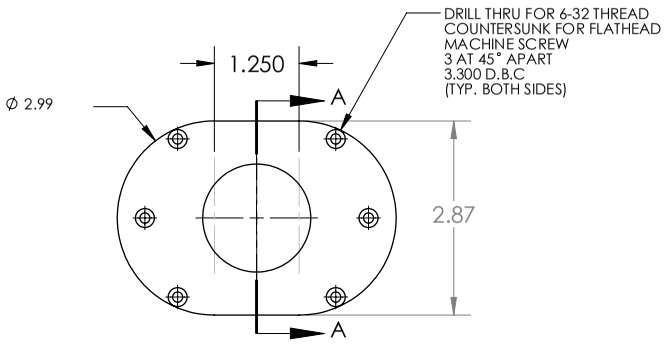

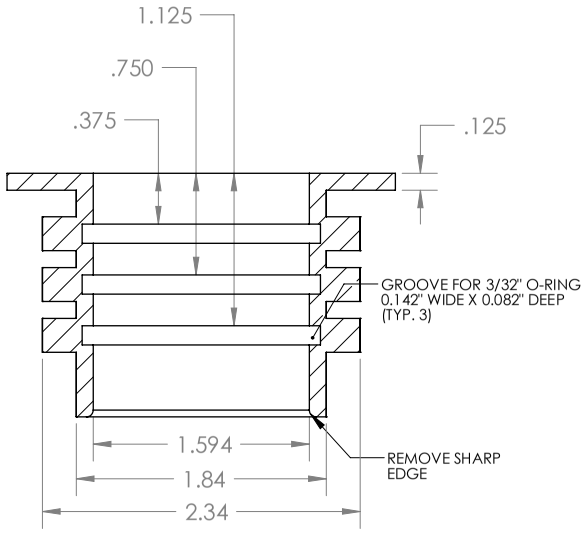

SECTION A-A
SCALE 1 : 1

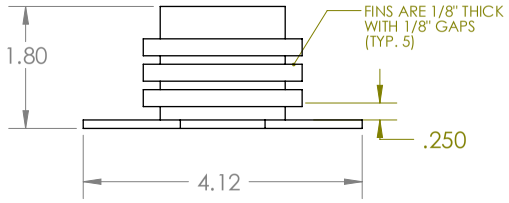

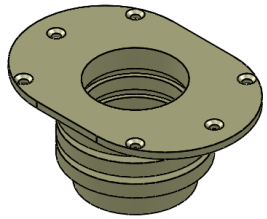

MATERIAL IS BRASS

TOLERANCE:
.x ±0.025
.xx ±0.01
.xxx ±0.005

TOP INSERT	
NAME: SILAS SMITH	05/06/2011
PHONE: 802-274-2602	

The University of Vermont

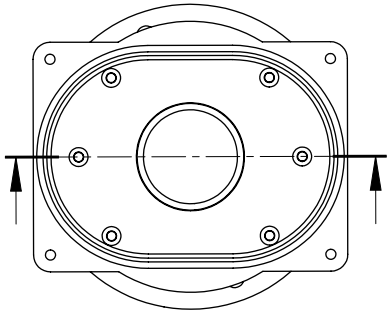

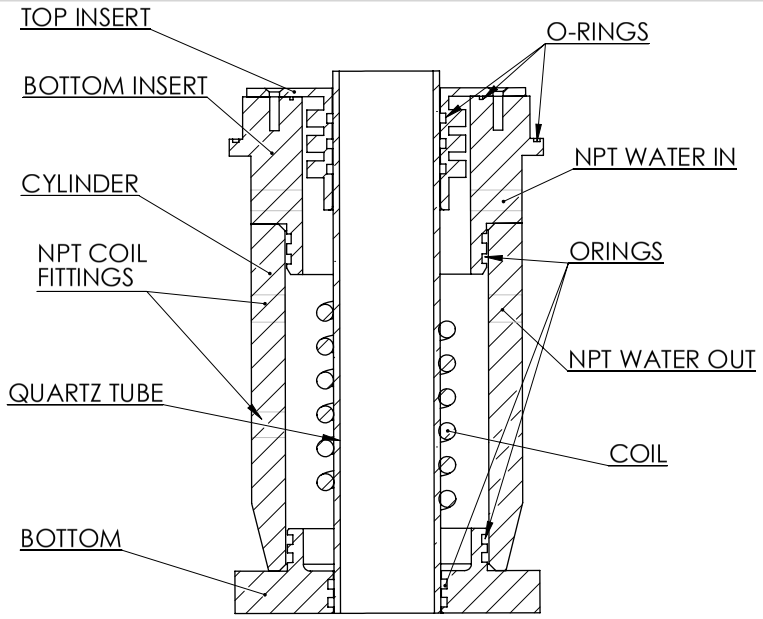

SECTION A-A

INJECTOR ASSEMBLY	
NAME: SILAS SMITH	06/18/2011
PHONE: 802-274-2602	

The University *of* Vermont

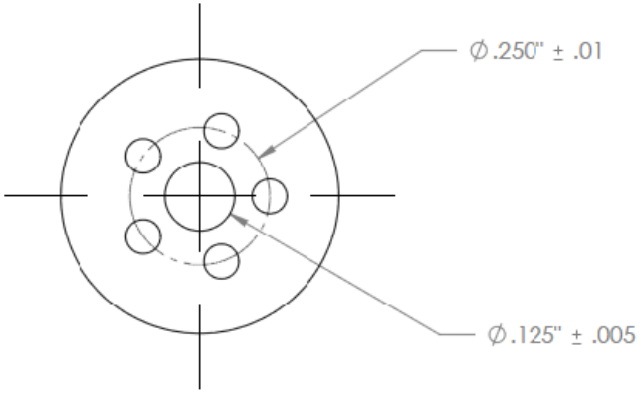

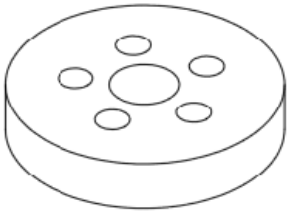

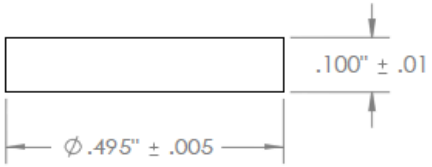

MATERIAL IS BRASS

TOLERANCE
.x ±0.025
.xx ±0.01
.xxx ±0.005

LID PROPOSAL	
NAME: SILAS SMITH	05/31/2012
PHONE: 802-274-2602	

The University of Vermont

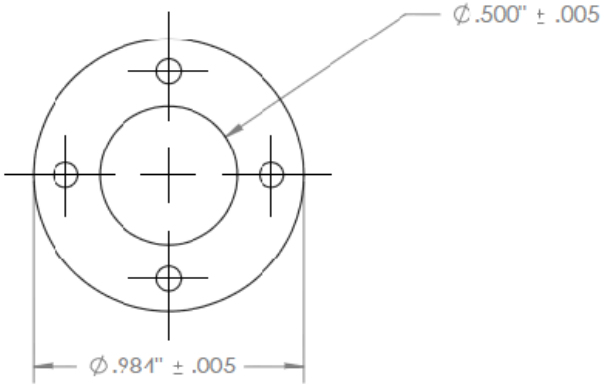

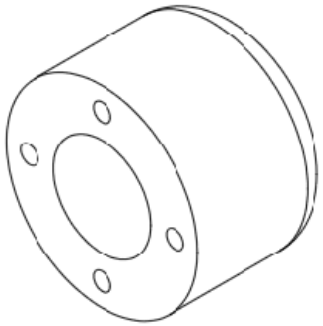

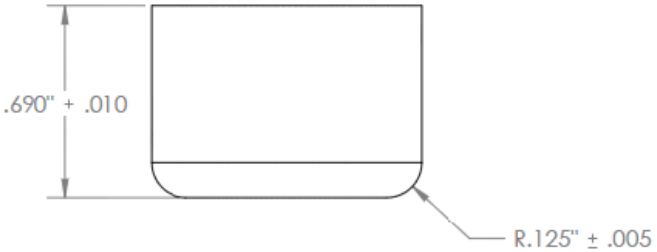

MATERIAL IS COPPER

TOLERANCE
.x ±0.025
.xx ±0.01
.xxx ±0.005

BOTTOM PROPOSAL	
NAME: SILAS SMITH	05/31/2012
PHONE: 802-274-2602	

The University of Vermont

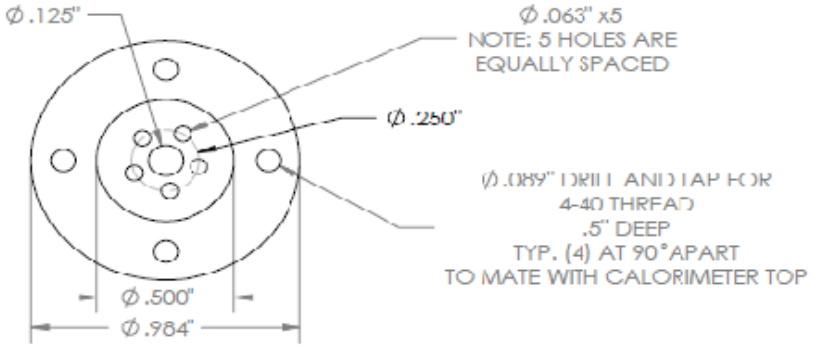

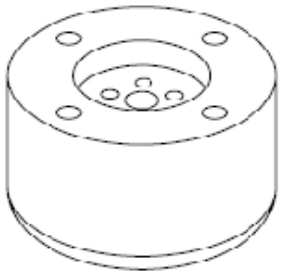

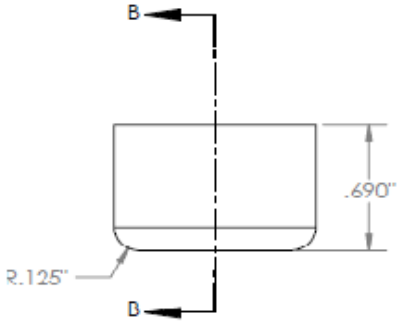

SECTION B-B

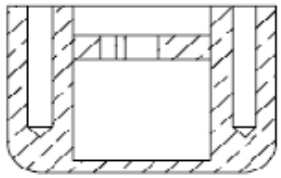

SECTION A-A
SCALE 1 : 1

TOLERANCE:
.x ±0.025
.xx ±0.01
.xxx ±0.005

CALORIMETER ASSEMBLY	
NAME: SILAS SMITH	09/18/2012
PHONE: 802-274-2602	

The University of Vermont

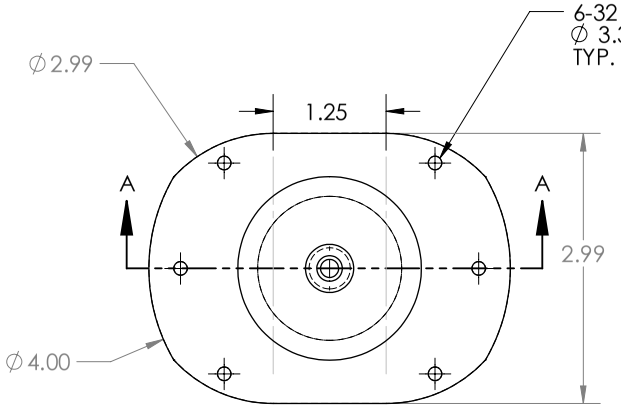

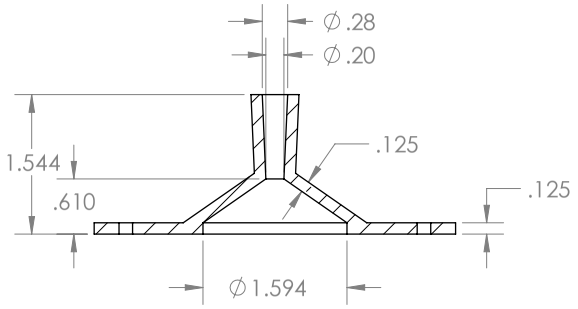

SECTION A-A
SCALE 1 : 1.5

MATERIAL IS ABS PLASTIC

TOLERANCE:
.x ±0.025
.xx ±0.01
.xxx ±0.005

1st ITERATION NOZZLE 0.20AR15	
NAME: SILAS SMITH	09/18/2012
PHONE: 802-274-2602	

The University *of* Vermont

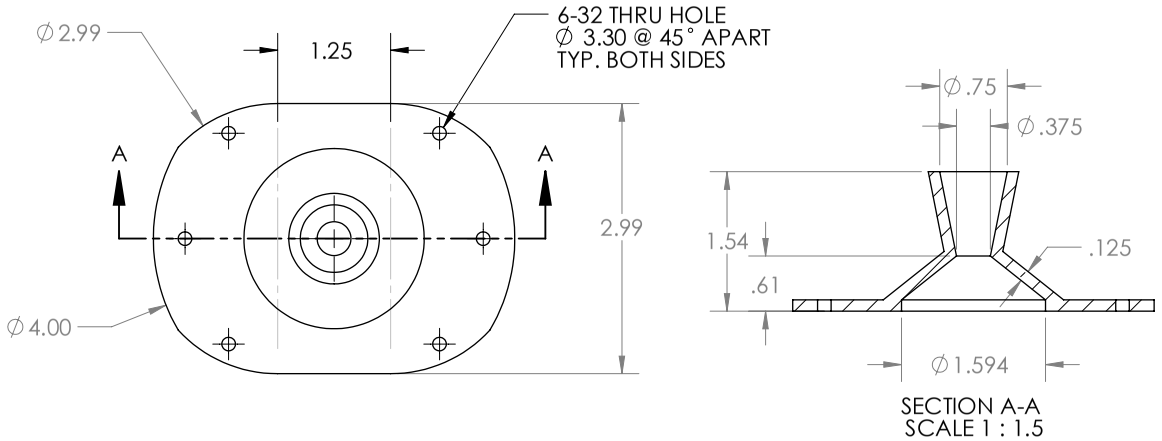

SECTION A-A
SCALE 1 : 1.5

MATERIAL IS ABS PLASTIC

TOLERANCE:
.x ±0.025
.xx ±0.01
.xxx ±0.005

1ST ITERATION NOZZLE 0.375AR2	
NAME: SILAS SMITH	09/18/2012
PHONE: 802-274-2602	

The University of Vermont

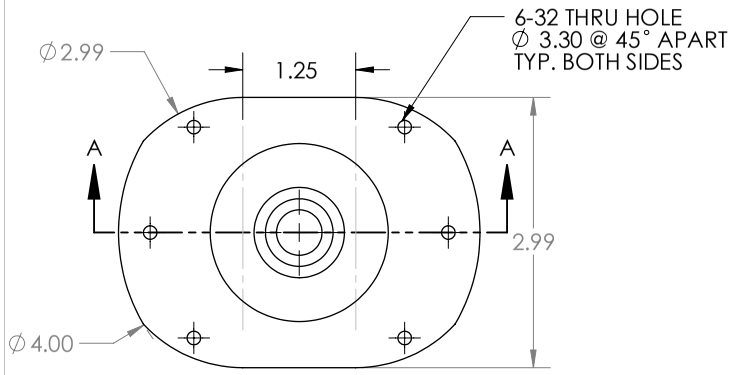

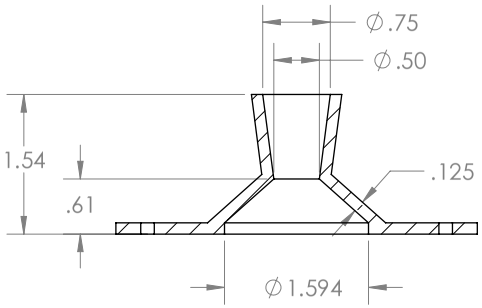

SECTION A-A

SCALE 1 : 1.5

MATERIAL IS ABS PLASTIC

TOLERANCE:
.x ±0.025
.xx ±0.01
.xxx ±0.005

1ST ITERATION NOZZLE 0.504AR2	
NAME: SILAS SMITH	09/18/2012
PHONE: 802-274-2602	

The University *of* Vermont

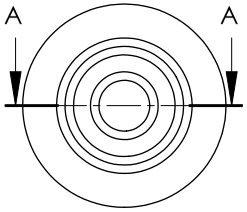

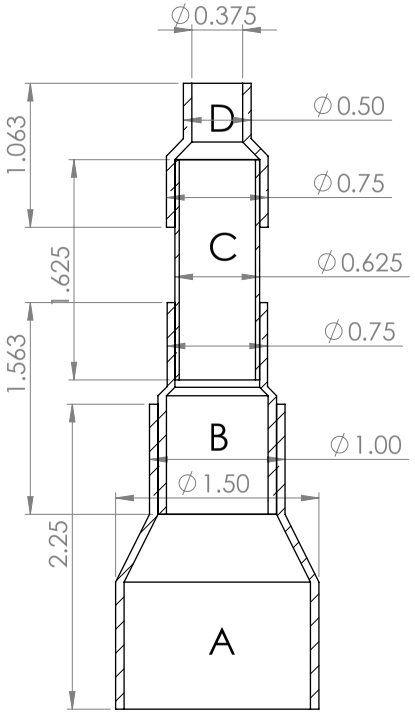

SECTION A-A
SCALE 1 : 1

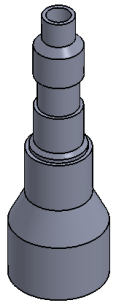

MATERIAL IS COPPER

TOLERANCE:
.x ±0.025
.xx ±0.01
.xxx ±0.005

PIPE COUPLING ASSEM	
NAME: SILAS SMITH	09/18/2012
PHONE: 802-274-2602	

The University of Vermont

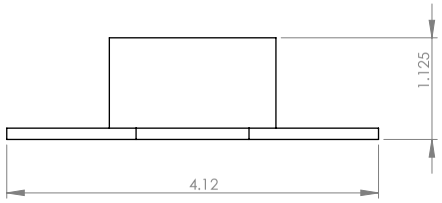

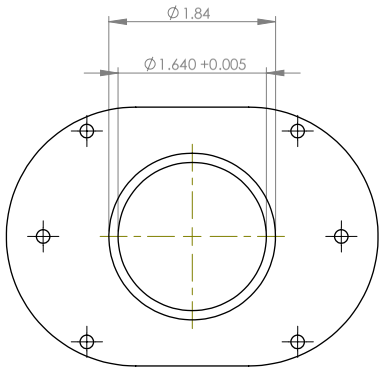

MATERIAL IS BRASS

TOLERANCE:
.x ±0.025
.xx ±0.01
.xxx ±0.005

NOTES:
MODIFY FROM EXISTING PART
ONLY THE DIMENSIONS SHOWN

BOTTOM SALVAGED TO MATE WITH
BASE NOZZLE (TIGHT SLIP FIT)

BOTTOM SALVAGED	
NAME: SILAS SMITH	12/04/2012
PHONE: 802-274-2602	

The University *of* Vermont

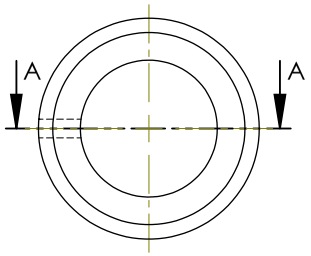

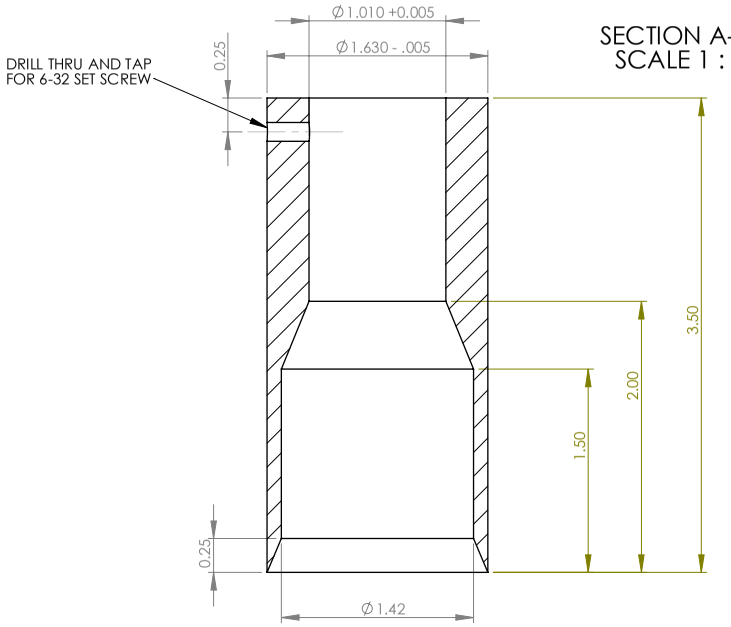

SECTION A-A
SCALE 1 : 1

MATERIAL IS COPPER

TOLERANCE:
.x ±0.025
.xx ±0.01
.xxx ±0.005

NOTES:
NOZZLE HOLDER TO MATE WITH
SSNOZZLE AND SALVAGED BOTTOM
(TIGHT SLIP FIT)

NOZZLE HOLDER	
NAME: SILAS SMITH	12/04/2012
PHONE: 802-274-2602	

The University *of* Vermont

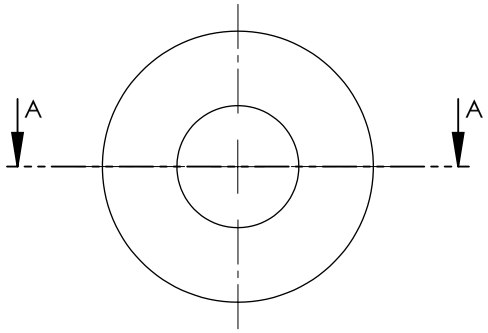

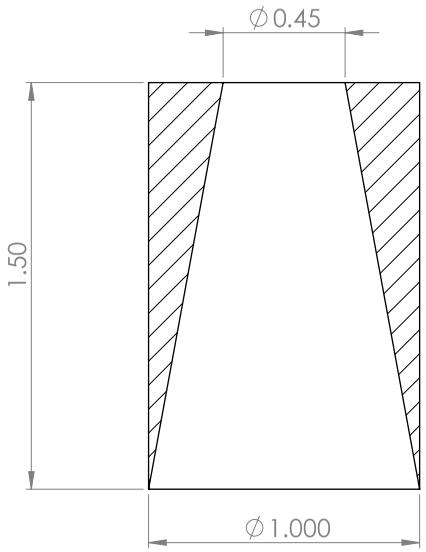

SECTION A-A
SCALE 2 : 1

MATERIAL IS COPPER

TOLERANCE:
.x ±0.025
.xx ±0.01
.xxx ±0.005

SONIC NOZZLE TO MATE WITH
NOZZLE HOLDER (TIGHT SLIP FIT)

SONICNOZZLE45	
NAME: SILAS SMITH	12/04/2012
PHONE: 802-274-2602	

The University of Vermont

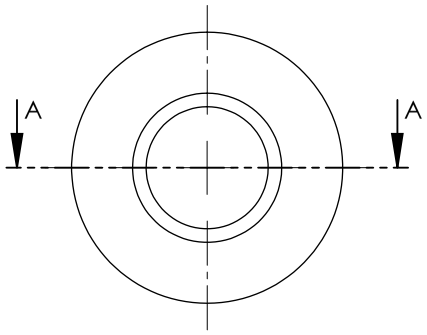

SECTION A-A
SCALE 2 : 1

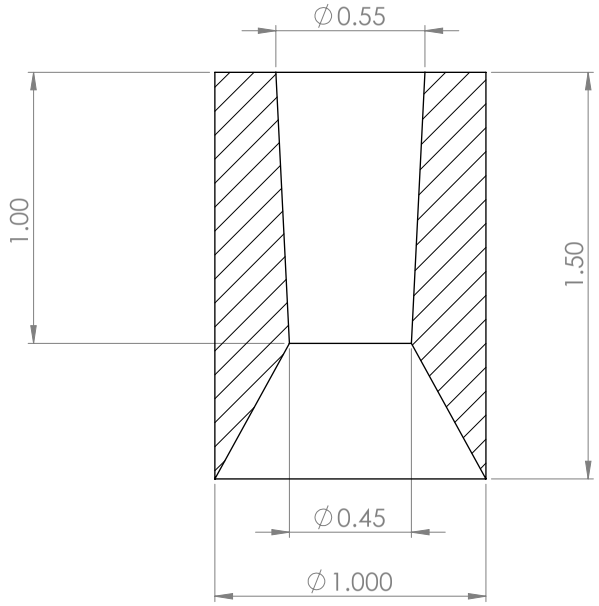

MATERIAL IS COPPER

TOLERANCE:
.x ±0.025
.xx ±0.01
.xxx ±0.005

SSNOZZLE TO MATE WITH
NOZZLE HOLDER
(TIGHT SLIP FIT)

SSNOZZLE45AR15	
NAME: SILAS SMITH	12/04/2012
PHONE: 802-274-2602	

The University *of* Vermont

```
clear all
close all
clc

%%% Image Processing    %%%
sonAr=imread('0040_1crop.jpg');

 sonArgry=rgb2gray(sonAr);
 sonAr_imadj=imadjust(sonArgry,[0.09; 0.11],[0;1]);
 sonArneg = imcomplement(sonAr_imadj);
 sonAredge = edge(sonArneg,'prewitt');
 rgb = imoverlay(sonAr,sonAredge,[0 0 1]);
subplot(1,3,1)
 imshow(sonAr)
 title('Raw Image')
 subplot(1,3,2)
 imshow(sonAredge)
 title('Bounding Edge')
 subplot(1,3,3)
 imshow(rgb)
title('Overlayed Image')
suptitle('Sonic Nozzle 30 [slm] Argon')
```

Matlab code used for exit angle detection.

30 [slm] Ar Supersonic Nozzle

Raw Image

Filtered Image

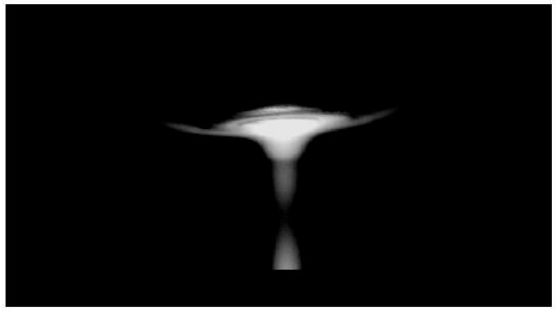

Raw Image

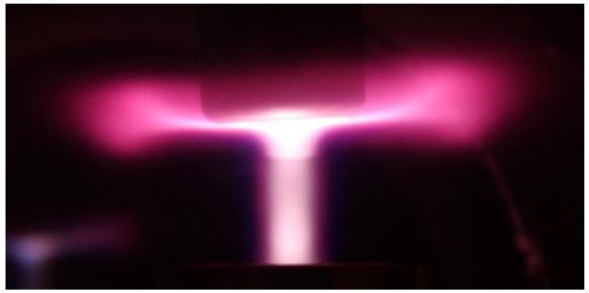

Filtered Image